



# A viscous vortex model for predicting the drag reduction of riblet surfaces

J. Wong<sup>1,†</sup>, C.J. Camobreco<sup>1</sup>, R. García-Mayoral<sup>2</sup>, N. Hutchins<sup>1</sup> and D. Chung<sup>1</sup>

<sup>1</sup>Department of Mechanical Engineering, University of Melbourne, Victoria 3010, Australia

<sup>2</sup>Department of Engineering, University of Cambridge, Cambridge CB2 1PZ, UK

(Received 17 March 2023; revised 9 October 2023; accepted 22 November 2023)

This paper introduces a viscous vortex model for predicting the optimal drag reduction of riblet surfaces, eliminating the need for expensive direct numerical simulations (DNSs) or experiments. The footprint of a typical quasi-streamwise vortex, in terms of the spanwise and wall-normal velocities, is extracted from smooth-wall DNS flow fields in close proximity to the surface. The extracted velocities are then averaged and used as boundary conditions in a Stokes-flow problem, wherein riblets with various cross-sectional shapes are embedded. Here, the same smooth-wall-based boundary conditions can be used for riblets, as we observe from the DNSs that the quasi-streamwise vortices remain unmodified apart from an offset. In particular, the position of these vortices remain unpinned above small riblets. The present approach is compared with the protrusion-height model of Luchini *et al.* (*J. Fluid Mech.*, vol. 228, 1991, pp. 87–109), which is also based on a Stokes calculation, but represents the vortex with only a uniform spanwise velocity boundary condition. The key novelty of the present model is the introduction of a wall-normal velocity component into the boundary condition, thus inducing transpiration at the riblet crests, which becomes relevant as the riblet size increases. Consequently, the present model allows for the drag-reduction prediction of riblets up to the optimal size. The present approach does not rely on the scale separation formally required by homogenisation techniques, which are only applicable for vanishingly small riblets.

**Key words:** drag reduction, turbulent boundary layers

## 1. Introduction

Energy-saving strategies for large transport systems play an important role in mitigating both rising energy costs and increasing carbon emissions. Large transport systems with slender bodies, e.g. ships (Schultz *et al.* 2011) and aircraft (Viswanath 2002),

† Email address for correspondence: [jeremy.wong@unimelb.edu.au](mailto:jeremy.wong@unimelb.edu.au)

primarily expend energy to overcome skin-friction drag. An approach for reducing the skin-friction drag is through the use of riblets. Riblets are intentionally roughened surfaces, streamwise-aligned micro-ribs that reduce drag below that of a smooth surface without energy input (Choi, Moin & Kim 1993; Bechert *et al.* 1997; García-Mayoral & Jiménez 2011*a*; von Deyn, Gatti & Frohnafel 2022). The optimal spacing of riblets on a passenger aircraft is of the order of 50–100  $\mu\text{m}$  (Viswanath 2002). Because of this small scale, the widespread use of riblets today is hampered by the complexity in manufacturing, maintenance and wear (Bushnell 2003; Choi 2013). Currently, it is uncertain whether the performance of imperfectly manufactured or worn riblet surfaces remains acceptable and, ultimately, cost effective across their lifespan. Particularly, the effect of riblet tip erosion on performance has not received enough attention, with two noteworthy experiments by Walsh (1982, 1990). To address the sensitivity of the performance change due to imperfections, a routine yet highly accurate predictive model is needed. Previously, a model was advanced by Luchini, Manzo & Pozzi (1991) and Luchini (1996) using the concept of Stokes-flow protrusion heights. The model predicts that riblets with sharp tips generally perform better (García-Mayoral & Jiménez 2011*a*), consistent with Walsh (1990). However, the magnitude of optimal drag reduction, which riblets attain at small but non-vanishing sizes, is overpredicted by the model. This is because the model was designed for vanishingly small riblets. Therefore, our aim is to develop a model to predict the optimal drag reduction that accounts for the additional effects of non-vanishing riblet sizes.

The paper is divided into two main parts. The first part (§§ 2–3) uses the present direct numerical simulation (DNS) dataset to assess riblet drag-reduction predictions based on the protrusion-height model by Luchini *et al.* (1991). The first part provides clear information to the second part (§ 4), which develops a new model that accurately predicts the drag reduction up to the optimal riblet size. Specifically, in § 2, we outline the method to obtain our present DNS dataset comprising several riblet shapes and sizes around the optimal. In § 3.1, we first show that, as expected, the protrusion-height model does not accurately predict the drag reduction for riblets of non-vanishing sizes. However, the DNSs demonstrate that the flow above riblets remains essentially an offset of the smooth-wall flow, as proposed by Luchini (1996), up to the optimal riblet size. Thus, the drag reduction (log-layer velocity difference  $-\Delta U^+$ ) can be quantified by the difference between the observed origin offsets of the mean flow  $\ell_U^+$  and the turbulence  $\ell_T^+$  (Gómez-de-Segura, Sharma & García-Mayoral 2018*b*). Further, the DNSs show that the Stokes-flow protrusion height for the streamwise flow  $h_{\parallel}^+$  remains an accurate prediction of  $\ell_U^+$ , whereas the protrusion height for the spanwise flow  $h_{\perp}^+$  becomes an increasingly inaccurate estimate of  $\ell_T^+$  for larger riblets (for notation, see table 1). In § 3.2, we demonstrate that the effect of wall-normal transpiration above non-vanishing riblets is crucial to predicting  $\ell_T^+$  accurately, as the  $\ell_T^+$  values of riblets agree with an empirical equation for  $\ell_T^+$  proposed by Ibrahim *et al.* (2021) that incorporates the effects of transpiration. However, the empirical equation is developed based on simulations with Robin boundary conditions and applying the empirical equation to riblets requires *a posteriori* measurements from the DNS. To circumvent the need for riblet DNSs, here, we develop a model that incorporates wall-normal transpiration effects, borrowing ideas and insights from models for quasi-streamwise vortices surveyed in § 3.3. In § 4, we discuss the development, methodology and validation of our present model based on a vortex flow structure representing turbulence to accurately predict  $\ell_T^+$  and, hence, the drag reduction up to the optimal size of riblets. In § 5, we conclude and discuss the outlook for the model.

## 2. Direct numerical simulation dataset

In this section, we discuss the methodology and validation of our present DNS dataset, which will allow us to assess the limitations of the model by Luchini *et al.* (1991) in § 3, and to develop the present model in § 4. The DNSs solve the Navier–Stokes equations using a commercial solver Cliff by Cascade Technologies Inc. (Ham, Mattsson & Iaccarino 2006; Ham *et al.* 2007). Cliff is a second-order accurate node-based collocated finite-volume incompressible-flow solver on unstructured grids. The code solves the following mass and momentum equations:

$$\nabla \cdot \mathbf{u} = 0, \quad \frac{\partial \mathbf{u}}{\partial t} + \nabla \cdot (\mathbf{u}\mathbf{u}) = -\frac{1}{\rho} \nabla p + \nu \nabla^2 \mathbf{u} - \frac{1}{\rho} \frac{dP}{dx} \mathbf{i}, \quad (2.1a,b)$$

where  $\mathbf{u} = (u, v, w)$  are the instantaneous fluid velocities in the streamwise,  $x$ , spanwise,  $y$ , and wall-normal,  $z$ , directions, respectively,  $t$  is time,  $p$  is the periodic (fluctuating) pressure,  $\rho$  is the fluid density,  $\nu$  is the kinematic viscosity,  $dP/dx$  is the driving pressure gradient term and  $\mathbf{i}$  is the streamwise unit vector. The total pressure  $p_T$  is decomposed into a mean (driving) and periodic pressure,  $p_T(x, y, z, t) = p(x, y, z, t) + P(x)$ , where  $P(x)$  is the input into our simulation through a spatially uniform body force. The boundary conditions are a no-slip smooth/riblet wall, periodic  $x$  and  $y$  boundaries and slip at the top of the domain, thus simulating an open-channel flow.

Conventional DNSs of wall-bounded turbulent flows use fine grids to resolve the small viscous scales, while a large domain is used to capture the large outer-layer motions. To statistically capture the flow behaviour, the size of the domain should be approximately  $L_x = 2\pi\delta$  and  $L_y = \pi\delta$  (Lozano-Durán & Jiménez 2014), where  $\delta$  is the half-channel height, or in viscous units,  $L_x^+ \approx 2500$  and  $L_y^+ \approx 1250$  for a friction Reynolds number  $Re_\tau = 395$ , where the ‘+’ superscript is the normalisation with friction velocity and kinematic viscosity  $\nu$ . For riblets, these simulations are costly because a large number of cells are needed near the wall to resolve the texture. This is typically 28–32 points per riblet spacing  $s^+$  for  $8 \lesssim s^+ \lesssim 50$ , resulting in a grid resolution of  $0.1 \lesssim \Delta_y^+ \lesssim 0.5$ , which is denser than a typical smooth-wall DNS ( $\Delta_y^+ \approx 3$ ). The high computational costs can be reduced through the use of minimal channels, which involves reducing the streamwise and spanwise dimensions of a conventional channel domain. Minimal channels containing the smooth-wall buffer layer turbulence were initially introduced by Jiménez & Moin (1991). Subsequently, Flores & Jiménez (2010) developed the minimal channels containing the smooth-wall logarithmic layer turbulence, which was further extended by Chung *et al.* (2015) to enable measurements of  $\Delta U^+$  for rough walls (MacDonald *et al.* 2017) and riblets (Endrikat *et al.* 2021b). By comparing the mean velocity profiles of minimal channels with those of conventional channels, accurate measurements of drag change can be obtained from a prespecified wall-normal range that extends up to a critical height  $z_c^+$ , which is proportional to the span of the channel,  $L_y^+$  (Flores & Jiménez 2010). Suggestions for  $z_c^+$  vary in the range of  $0.3L_y^+ \lesssim z_c^+ \lesssim 0.4L_y^+$  (Flores & Jiménez 2010; Chung *et al.* 2015; MacDonald *et al.* 2017). For the size of our minimal domain, we choose the spanwise length  $L_y^+ \gtrsim 250$  (same as the smooth-wall reference minimal-channel case). Thus,  $z_c^+ \gtrsim 100$ , so that the log region is accurately captured and  $\Delta U^+$  (i.e. the velocity difference in the log region) can be measured. A detailed measurement of  $\Delta U^+$  is outlined in Appendix A. We also set the streamwise length  $L_x^+ \gtrsim 1000$ , sufficient to capture the streamwise streaks, as suggested by MacDonald *et al.* (2017).

Protrusion heights	$h_{\parallel}, h_{\perp}$	Extrapolated origins from Stokes-flow calculations
Slip/transpiration lengths	$\ell_x, \ell_y, \ell_z$	Prescribed at the wall for a Robin boundary condition
Virtual origins	$\ell_u, \ell_v, \ell_w$	Observed origins of (direct numerical simulation) root-mean-squared velocity profiles
Mean virtual origin	$\ell_U$	Observed origin of (direct numerical simulation) mean profile
Turbulent virtual origin	$\ell_T$	Observed origin of (direct numerical simulation) Reynolds shear stress profile

Table 1. Summary of lengths used in this paper and how they are obtained. For consistency with the literature, we use  $h$  for those quantities proposed by Luchini *et al.* (1991), and  $\ell$  for those from Ibrahim *et al.* (2021).

Table 2 reports the riblet flow cases and the reference smooth-wall cases. All cases are run at a friction Reynolds number of  $Re_{\tau} = 395$ , except for one smooth-wall case (S1000) at  $Re_{\tau} = 1000$ . The case IDs with an asterisk (\*) are from Endrikat *et al.* (2021*a,b*, 2022) and Modesti *et al.* (2021). For the larger riblets, for which data overlap permits comparison, these DNSs demonstrate good agreement with experimental results, including spectra and time-averaged flow within the grooves (Endrikat *et al.* 2022). For minimal channels (Flores & Jiménez 2010; MacDonald *et al.* 2017), the largest eddy turnover time,  $L_t u_{\tau} / z_c$ , i.e. the simulation time  $L_t$  normalised by the characteristic period of the largest resolved turbulent scale  $z_c / u_{\tau}$ , is chosen to ensure that the uncertainty in the measured  $\Delta U^+$  is small following the guidelines established by MacDonald *et al.* (2017)

$$L_t \frac{u_{\tau}}{z_c} \approx 6 \left( \frac{91.4}{\zeta^+ z_c^+} \right)^2 \frac{7.5 z_c}{L_x} \frac{2.5 z_c}{L_y}, \tag{2.2}$$

where  $\zeta^+$  is the uncertainty in the measured  $\Delta U^+$ . Given our minimal domain, gathering statistics for roughly  $L_t u_{\tau} / z_c \approx 300$  eddy turnover times after transients decay is sufficient to ensure  $\zeta^+ \approx \pm 0.1$  (table 2), except for the cases with longer streamwise domain length,  $L_x^+ \approx 2000$ , where  $L_t u_{\tau} / z_c \approx 125$  eddy turnovers are sufficient. These eddy turnover times based on eddy counts (MacDonald *et al.* 2017) are corroborated by a statistical convergence study for riblets by Endrikat *et al.* (2021*b*): statistics that are considered converged based on the  $L_t u_{\tau} / z_c$  criteria above typically exhibited differences of  $\lesssim 1\%$  between the measured  $(x, y, t)$ -averaged shear stress and the linear profile (cf. Vinuesa *et al.* 2016).

The friction velocity can be obtained from two methods: (i) the nominal friction velocity,  $u_*$ , i.e. the drag on the riblet wall per plan area (not wetted area), derived *a priori* from the force balance of the domain, or (ii) the effective friction velocity,  $u_{\tau}$ , measured *a posteriori* at the virtual origin of turbulence,  $z^+ = -\ell_T^+$  (Gómez-de-Segura *et al.* 2018*a*; Fairhall, Abderrahaman-Elena & García-Mayoral 2019; Ibrahim *et al.* 2021), outlined in detail in Appendix A. For the cases considered in table 2,  $u_*$  and  $u_{\tau}$  differ only by a maximum of 1%. However,  $\Delta U^+$  differs by approximately 10% up to the optimum size based on these two friction velocities. Following the rationale of Ibrahim *et al.* (2021), we use  $u_{\tau}$  when measuring  $\Delta U^+$ , which we report in table 2.

We carry out additional small riblet simulations, at  $\ell_g^+ \approx 5, 8$  and 10, where  $\ell_g^+$  is the square root of the riblet groove area (see sketches in table 2), to fill the viscous parameter space beyond Endrikat *et al.* (2021*b*). The additional cases also utilise an adaptive mesh refinement tool (Adapt) to refine the mesh near the wall and resolve the riblet texture, while the mesh farther from the wall is coarser for computational efficiency yet sufficiently fine

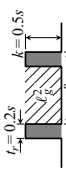

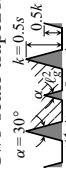
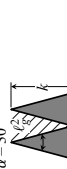
Riblet	Case	$s^+$	$\ell_g^+$	$k/\delta$	$\Delta_x^+$	$\Delta_{y,min}^+ - \Delta_{y,max}^+$	$\Delta_{z,min}^+ - \Delta_{z,max}^+$	$L_x^+$	$L_y^+$	$\Delta_t^+ \times 10^3$	$\Delta U^+ \pm \zeta^+$
 Blade $\alpha = 0.2s$ $k = 0.5s$	BL08	7.8	4.9	0.010	6.0	0.195-0.781	0.304-7.000	1002	250	47.4	-0.46 ± 0.10
	BL12	11.9	7.5	0.015	6.0	0.298-1.191	0.320-7.000	1002	250	47.4	-0.67 ± 0.10
	BL16	15.6	9.9	0.020	6.0	0.391-1.563	0.385-7.000	1002	250	47.4	-0.81 ± 0.10
	BL20*	20.3	12.8	0.026	6.0	0.510-2.100	0.270-6.100	1027	264	47.4	-0.75 ± 0.10
	BL25	25.0	15.8	0.032	6.0	0.625-2.500	0.295-7.000	1002	250	47.4	-0.36 ± 0.11
BL33*	33.3	21.1	0.042	6.0	0.830-3.400	0.280-6.300	1027	266	47.4	0.71 ± 0.10	
 Trapezoidal $\alpha = 30^\circ$ $k = 0.5s$	TA08	7.5	5.0	0.010	6.0	0.027-0.758	0.039-6.991	1002	250	47.4	-0.72 ± 0.11
	TA11	11.4	7.5	0.014	6.0	0.041-1.136	0.058-6.905	1002	250	47.4	-1.09 ± 0.09
	TA15	14.7	9.7	0.019	6.0	0.053-1.471	0.075-6.972	1002	250	47.4	-1.27 ± 0.09
	TA18	17.9	11.8	0.023	6.0	0.064-1.786	0.093-6.958	1002	250	47.4	-1.24 ± 0.11
	TA23	22.7	15.0	0.029	6.0	0.073-2.552	0.116-6.888	1002	250	47.4	-0.86 ± 0.10
TA31*	31.3	20.6	0.040	6.0	0.470-2.400	0.310-7.000	2054	250	47.4	0.55 ± 0.10	
 Two-scale trapezoidal $\alpha = 30^\circ$ $k = 0.5s$	TM13*	12.5	6.9	0.016	6.0	0.087-1.563	0.024-7.059	2054	250	19.8	-0.89 ± 0.11
	TM17*	16.7	9.3	0.021	6.0	0.064-2.084	0.031-7.027	2054	250	13.8	-1.03 ± 0.11
	TM21*	20.8	11.6	0.026	6.0	0.087-2.604	0.040-7.108	2054	250	15.8	-1.06 ± 0.11
	TM25*	25.0	13.9	0.032	6.0	0.108-3.125	0.047-7.076	2054	250	15.8	-0.81 ± 0.11
	TM31*	31.3	17.3	0.040	6.0	0.145-1.885	0.059-7.028	2054	250	23.7	-0.23 ± 0.11
TM36*	36.5	20.2	0.046	6.0	0.177-2.195	0.070-7.102	2054	255	27.6	0.24 ± 0.11	
TM42*	41.7	23.1	0.053	6.0	0.209-2.507	0.079-7.061	2054	250	27.6	0.58 ± 0.10	
 30° triangle $\alpha = 30^\circ$	T308	7.8	7.5	0.037	6.0	0.085-0.781	0.051-6.941	1002	250	47.4	-0.81 ± 0.12
	T310*	10.1	9.8	0.048	6.0	0.019-0.360	0.033-7.000	1027	252	15.8	-1.03 ± 0.12
	T313	12.5	12.1	0.059	6.0	0.136-1.250	0.073-6.973	1002	250	47.4	-1.00 ± 0.13
	T321*	21.1	20.4	0.100	6.0	0.120-3.200	0.023-6.900	1027	253	15.8	0.85 ± 0.12

Table 2. For caption see next page.

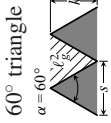
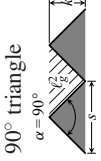
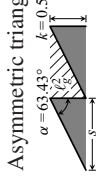
Riblet	Case	$s^+$	$l_g^+$	$k/\delta$	$\Delta_x^+$	$\Delta_{y,min}^+ - \Delta_{y,max}^+$	$\Delta_{z,min}^+ - \Delta_{z,max}^+$	$L_x^+$	$L_y^+$	$\Delta_t^+ \times 10^3$	$\Delta U^+ \pm \zeta^+$	
 60° triangle $\alpha = 60^\circ$	T611	11.4	7.5	0.025	6.0	0.036–1.136	0.020–6.955	1002	250	47.4	$-0.81 \pm 0.11$	
	T615*	14.7	9.7	0.032	6.0	0.083–2.200	0.041–7.000	1027	250	31.6	$-0.98 \pm 0.10$	
	T618	17.9	11.8	0.039	6.0	0.143–1.786	0.044–6.921	1002	250	47.4	$-0.95 \pm 0.11$	
	T635*	35.0	23.0	0.077	6.0	0.026–1.094	0.014–4.651	1027	245	23.7	$0.72 \pm 0.10$	
	T910	10.0	5.0	0.013	6.0	0.027–1.000	0.021–6.934	1002	250	47.4	$-0.46 \pm 0.11$	
 90° triangle $\alpha = 90^\circ$	T915	14.7	7.4	0.019	6.0	0.041–1.471	0.030–6.894	1002	250	47.4	$-0.60 \pm 0.10$	
	T919*	19.2	9.6	0.024	6.0	0.110–2.900	0.047–7.059	1027	250	47.4	$-0.72 \pm 0.08$	
	T925	25.0	12.5	0.032	6.0	0.070–2.500	0.052–6.938	1002	250	47.4	$-0.37 \pm 0.10$	
	T950*	50.0	25.0	0.063	6.0	0.300–7.100	0.029–7.000	1027	250	47.4	$1.05 \pm 0.10$	
	AT10	10.0	5.0	0.013	6.0	0.049–1.000	0.077–6.905	1008	250	47.4	$-0.42 \pm 0.12$	
 Asymmetric triangle $\alpha = 63.43^\circ$ , $k = 0.5s$	AT15*	14.7	7.4	0.019	6.5	0.219–2.000	0.119–5.788	1027	250	47.4	$-0.53 \pm 0.14^\dagger$	
	AT19*	19.2	9.6	0.024	6.5	0.208–1.879	0.042–5.770	1027	250	47.4	$-0.60 \pm 0.09$	
	AT23	22.7	11.4	0.029	6.0	0.162–2.273	0.066–6.966	1008	250	47.4	$-0.48 \pm 0.10$	
	AT31*	31.3	15.6	0.040	6.5	0.107–4.305	0.029–5.710	1027	250	47.4	$-0.29 \pm 0.14$	
	AT42*	41.7	20.8	0.053	6.5	0.314–2.660	0.022–4.946	1027	250	47.4	$0.29 \pm 0.09$	
	S395*	—	—	—	6.0	3.0	0.210–4.700	0.210–4.700	1027	250	79.0	—
	SF395*	—	—	—	6.5	3.2	0.270–4.400	0.270–4.400	2482	1241	83.0	—
S1000*	—	—	—	6.0	3.0	0.320–8.800	0.320–8.800	2000	600	80.0	—	

Table 2. Riblet DNS cases. Existing cases (\*) are from Endrikat *et al.* (2021a, 2022) and Modesti *et al.* (2021). All cases are run at  $Re_\tau = 395$ , except for S1000 at  $Re_\tau = 1000$ . The roughness function,  $\Delta U^+$ , is measured from the mean velocity difference relative to the smooth wall, averaged in the range  $50 \lesssim z^+ \lesssim 100$ , except for case AT15 (marked by †), where we average the velocity difference in the range  $30 \lesssim z^+ \lesssim 50$ , due to a lower quality grid that causes a small underestimation of the mean velocity above  $z^+ \approx 50$ .



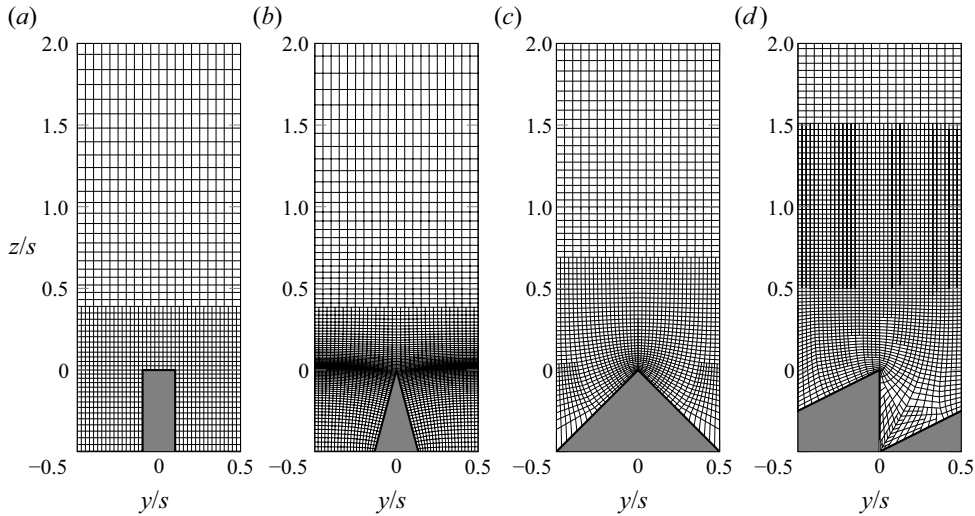


Figure 1. Streamwise uniform riblet mesh visualisation near the wall for present (non-asterisk) cases in [table 2](#). Grid-line intersections represent locations of nodes, which are closely packed near the wall ( $0.1 \lesssim \Delta_y^+ \lesssim 0.5$ ) and are coarsened further from the wall (21 points per riblet spacing,  $0.5 \lesssim \Delta_y^+ \lesssim 2$ ), and further coarsened near the top boundary (11 points per riblet spacing,  $1 \lesssim \Delta_y^+ \lesssim 3$ , not shown in figure above). Riblet cross-sectional geometries shown are (a) , (b) , (c) and (d) .

to resolve all turbulent flow scales. [Figure 1](#) illustrates some of the computational grids from the current cases (non-asterisk case IDs in [table 2](#)). Near the crests, there are  $n_s = 41$  points per riblet spacing, resulting in a spanwise grid size in the range of  $0.1 \lesssim \Delta_y^+ \lesssim 0.5$ . These grid specifications are similar or more refined than previous riblet DNSs, utilising at least  $n_s = 24$  points per riblet spacing (Goldstein, Handler & Sirovich 1995; Goldstein & Tuan 1998; García-Mayoral & Jiménez 2011b). The mesh is coarsened to  $n_s = 21$  ( $0.5 \lesssim \Delta_y^+ \lesssim 2$ ), starting from  $z^+ \approx k^+$  for the blade, trapezoidal and triangular riblets, or starting from  $z^+ \approx 3k^+$  for the asymmetric triangular riblets ([figure 1](#)). Above  $z^+ \approx 7k^+$ , the mesh is still finer than typical smooth-wall DNSs with  $1 \lesssim \Delta_y^+ \lesssim 3$  ( $n_s = 11$ ). The streamwise grid spacing is approximately the same for all cases in [table 2](#) ( $\Delta_x^+ \approx 6$ ), finer than typical smooth-wall DNSs. Overall, these grid sizes ( $\Delta_x^+$  and  $\Delta_y^+$ ) are also in line with previous riblet DNSs, where  $\Delta_x^+ \leq 9$  and  $\Delta_y^+ \leq 4$  (García-Mayoral & Jiménez 2011b, 2012). Furthermore, from the grid convergence study by Endrikat *et al.* (2021b), the grid used for T950 ( $n_s = 33$ ,  $\Delta_x^+ = 6$  and  $0.3 \lesssim \Delta_y^+ \lesssim 7.1$  in [table 2](#)) has been previously shown to achieve convergence in terms of the mean velocity, turbulent stresses and energy spectra, by comparing against two coarser grids, and one finer grid than that of T950. The grid resolutions of the present cases are either similar to or finer than that of T950.

The aforementioned computational demands of conventional DNSs, coupled with the requisite fine grids near the wall, resulted in limited studies in the past (e.g. El-Samni, Chun & Yoon 2007; García-Mayoral & Jiménez 2011a,b, 2012), although experimental data are available (e.g. Choi 1989; Bechert *et al.* 1997; Grüneberger & Hage 2011; von Deyn *et al.* 2022). For the previous small riblet DNS cases, Choi *et al.* (1993) reported results for triangle riblets with tip angles of  $60^\circ$  () and  $90^\circ$  (), and with  $\ell_g^+ \approx 14$  and 10, respectively. However, these cases were not fully resolved in the streamwise direction ( $\Delta_x^+ \approx 35$ ). More recently, El-Samni *et al.* (2007) performed

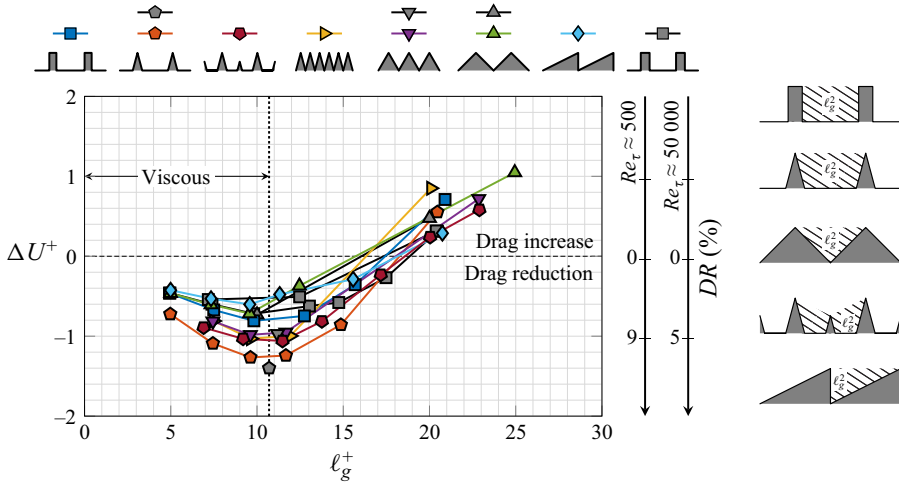


Figure 2. Riblet drag-reduction performance  $DR$  (right axis) or roughness function  $\Delta U^+$  (left axis) as a function of the square root of riblet groove area  $\ell_g^+$ . Axes on the right show the estimated percentage drag reduction,  $DR$  converted from  $\Delta U^+$  using (2.6) of Spalart & McLean (2011), based on typical laboratory or DNS conditions ( $Re_\tau \approx 500$ ), and typical aircraft fuselage conditions ( $Re_\tau \approx 50\,000$ ). In the viscous regime, the smooth-wall turbulent structures are not disrupted by the small textures, apart from their wall-normal displacement relative to the mean flow, and thus  $-\Delta U^+$  is the difference between the observed mean-flow origin and the turbulence origin (Gómez-de-Segura *et al.* 2018*b*), which increases with size (Bechert *et al.* 1997) up to a shape-independent size of  $\ell_g^+ \approx 10.7 \pm 1$  (García-Mayoral & Jiménez 2011*b*). Grey markers are data extracted from the mean profiles of (■) García-Mayoral & Jiménez (2011*b*, 2012), (◐) Bannier *et al.* (2015) and (▼) Malathi *et al.* (2022). Data from (▲) Li & Liu (2019) are extracted based on their  $DR$  values and converted to  $\Delta U^+$ . Coloured markers are present DNS data from table 2.


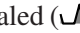
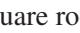
DNSs of thin blade riblets (└└└) which showed similar results to experimental data by Bechert *et al.* (1997). García-Mayoral & Jiménez (2011*a,b*, 2012) ran DNSs of thicker blade riblets (└└└,  $k/s = 0.5$ ,  $t_r/s = 0.25$ ,  $5 \lesssim \ell_g^+ \lesssim 25$ ) at  $Re_\tau = 180$  and 550 and reported similar  $\Delta U^+$  values (at matched  $\ell_g^+$ ) between the two  $Re_\tau$ . Figure 2 shows that the measured  $\Delta U^+$  values from table 2 are in good agreement with numerical data from past studies. Data from García-Mayoral & Jiménez (2011*b*, 2012) show similar trends with our present blade riblets. Li & Liu (2019) and Malathi *et al.* (2022) carried out boundary-layer DNSs for triangular riblets (▲▲▲ and ▲▲▲, respectively), the same as DNSs of Choi *et al.* (1993). The percentage drag reduction from Li & Liu (2019) was converted to  $\Delta U^+$ , whilst  $\Delta U^+$  from Malathi *et al.* (2022) was found directly from their mean profiles. These data agree well with our triangular riblet data (▲▼, figure 2), further validating the present DNS solver, minimal-channel approach and grid resolution choices. Finally, Bannier, Garnier & Sagaut (2015) performed wall-resolved large eddy simulation (LES) on trapezoidal riblets (└└└) with  $\ell_g^+ \approx 10.7$ . They reported  $\Delta U^+ \approx -1.4$  (◐, figure 2), which is larger by 10% compared with our trapezoidal riblet at  $\ell_g^+ \approx 10$ . We would expect a smaller percentage difference at matched size. There are no existing data in the literature for comparison for the other geometries (i.e. ▲▲▲▲▲, └└└└└). Notably, for the two-scale trapezoidal riblet simulations (└└└└└), Endrikat *et al.* (2022) found that the maximum attainable drag reduction is unaffected by the secondary riblet. Endrikat *et al.* (2022) also characterised the appropriate size of  $\ell_g^+$  for these two-scaled trapezoidal riblets.



### 3. Drag reduction of riblets in light of DNS data

#### 3.1. Drag reduction in terms of Stokes-flow protrusion heights and observed virtual origins

Luchini *et al.* (1991) and Luchini (1996) advanced a model for predicting riblet drag reduction using viscous (Stokes) flow. The model predicts the roughness function  $\Delta U^+$ , which is related to the drag reduction  $DR$ , quantified by the fractional change in skin-friction coefficient  $C_f$  relative to a baseline smooth wall,  $DR \equiv 1 - C_f/C_{f0}$ , where subscript 0 refers to the smooth wall. The roughness function  $\Delta U^+$  is given by  $\Delta U^+ = U_{\delta 0}^+ - U_{\delta}^+$  at matched  $Re_{\tau}$ , where  $U_{\delta}^+$  is the mean velocity at the edge ( $z = \delta$ ) of the wall-bounded turbulence. Since  $C_f \equiv 2/U_{\delta}^{+2}$ , we can relate  $DR$  and  $\Delta U^+$  at matched  $\delta^+ = Re_{\tau}$  by  $DR = 1 - (1 - \Delta U^+/U_{\delta 0}^+)^{-2} \sim -2\Delta U^+/U_{\delta 0}^+$  for small drag changes, or equivalently,  $DR \sim -(2C_{f0})^{1/2}\Delta U^+$  (Spalart & McLean 2011; García-Mayoral, Gómez-de-Segura & Fairhall 2019). Figure 2 demonstrates the conversion between  $\Delta U^+$  and  $DR$  for two values of  $Re_{\tau}$ .

Figure 2 shows  $\Delta U^+$  of conventionally shaped riblets (e.g. ) after Bechert *et al.* (1997), and of asymmetrical () and two-scaled () geometries as a function of the riblet size. The size is characterised by the square root of the riblet groove cross-sectional area,  $\ell_g^+$ , as defined on the right of figure 2. By using  $\ell_g^+$ , the optimal (maximum) drag reduction occurs at a shape-independent size of  $\ell_{g,opt}^+ \approx 10.7 \pm 1$  (García-Mayoral & Jiménez 2011a,b). For riblets below the optimal size ( $\ell_g^+ \lesssim 10.7$ ),  $-\Delta U^+$  increases with  $\ell_g^+$ . To predict this trend, Luchini *et al.* (1991) and Luchini (1996) proposed a linear viscous model for  $-\Delta U^+$  designed for vanishingly small riblets ( $\ell_g^+ \rightarrow 0$ )

$$-\Delta U^+ \approx \mu_0(h_{\parallel}^+ - h_{\perp}^+) = \mu_0(h_{\parallel}/\ell_g - h_{\perp}/\ell_g)\ell_g^+, \quad (3.1)$$

where  $h_{\parallel}$  and  $h_{\perp}$  are the Stokes-flow protrusion heights to locate the virtual origins perceived by streamwise and spanwise motions (velocities), respectively. The protrusion heights scaled by the riblet size,  $h_{\parallel}/\ell_g$  and  $h_{\perp}/\ell_g$ , can be routinely obtained from Stokes-flow calculations for a given riblet shape (Luchini *et al.* 1991; Bechert *et al.* 1997; Grüneberger & Hage 2011; García-Mayoral & Jiménez 2011a), and the protrusion-height difference ( $h_{\parallel}/\ell_g - h_{\perp}/\ell_g$ ) expresses the effect of riblet shape on the drag performance. The proportionality constant,  $\mu_0$  in (3.1), relates the protrusion heights to  $-\Delta U^+$ . The ansatz of Luchini (1996) implies  $\mu_0 = 1$ . However, the empirical values,  $\mu_0 = 0.785$  (Bechert *et al.* 1997; Grüneberger & Hage 2011) and  $\mu_0 = 0.66$  (Jiménez 1994; García-Mayoral & Jiménez 2011b) have also been used. Figure 3(a) shows  $\Delta U^+$  compensated by the respective  $h_{\parallel}/\ell_g - h_{\perp}/\ell_g$  and compares these DNS results with (3.1) using the aforementioned values of  $\mu_0$ . Here, the 30% scatter in  $\mu_0$  from the literature is reproduced by the present DNS data for riblets sizes up to  $\ell_g^+ \approx 8$ . This scatter suggests that  $\mu_0 < 1$  may be based on the  $\Delta U^+$  of non-vanishing riblet sizes that departs from the linear trend of (3.1). Towards vanishingly small riblet sizes ( $\ell_g^+ \approx 5$ ), discrepancies for different geometries are small and tend towards  $\mu_0 = 1$ , consistent with Luchini (1996). However, we observe typical departures from linearity of (3.1) near the optimum ( $\ell_g^+ \approx 10.7$ ). Extrapolating (3.1) to the optimal size overpredicts the drag reduction by up to 40% (figure 3a). For riblets, which yield small drag changes, such overprediction is especially undesirable. To account for this departure at the optimum ( $\ell_{g,opt}^+$ ), García-Mayoral & Jiménez (2011a) introduced an empirical constant 0.83 when evaluating  $DR$  and (3.1),

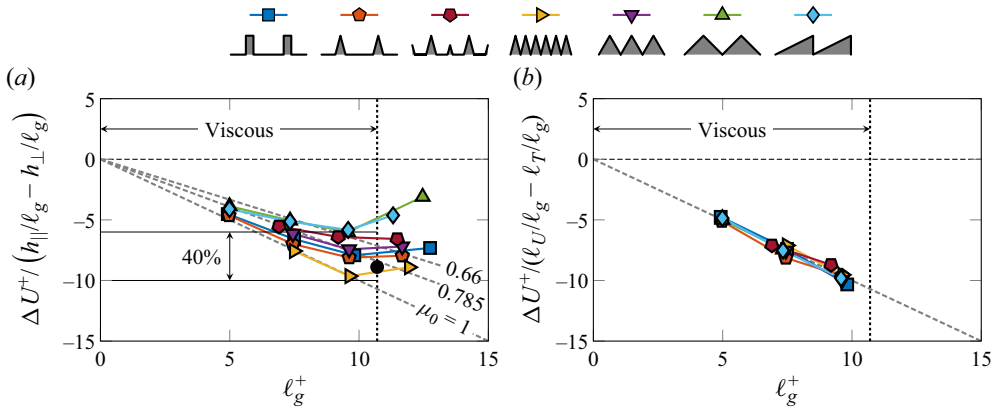


Figure 3. (a) Roughness function  $\Delta U^+$  normalised by the protrusion-height difference,  $h_{||}/\ell_g - h_{\perp}/\ell_g$ , reproduces a scatter in  $\mu_0$  from (3.1), which is consistent with the scatter in  $\mu_0$  in the literature (indicated by the dashed grey lines). Black marker ( $\bullet$ ) in (a) is an approximation of  $DR_{max}$  by García-Mayoral & Jiménez (2011a,b) using  $\mu_0 = 1$ . (b) Value of  $\Delta U^+$  normalised by the difference of the mean and turbulence virtual origins,  $\ell_U/\ell_g - \ell_T/\ell_g$  from (3.2) shows a smaller scatter than the protrusion-height normalisation shown in (a).

$DR_{max} = (2C_{f0})^{1/2} 0.83 \mu_0 (h_{||}/\ell_g - h_{\perp}/\ell_g) \ell_{g,opt}^+$  ( $\bullet$ , figure 3a). However, the data in figure 3(a) indicate that this empirical constant has a 20 % discrepancy.

Using the present DNS dataset, we will next review and assess the physical idea behind the aforementioned discrepancies. The Stokes-flow protrusion heights ( $h_{||}^+$  and  $h_{\perp}^+$ ) in (3.1) are meant to capture the observed virtual origins of the mean flow ( $\ell_U^+$ ) and turbulence ( $\ell_T^+$ ), respectively. In fact, figure 3(b) shows that it is the difference in the observed virtual origins,  $\ell_U^+ - \ell_T^+$  (measured *a posteriori* from DNS data), that better quantifies  $-\Delta U^+$ . These virtual origins are illustrated in figure 4. Here, the quasi-streamwise vortices, which represent the turbulence, perceive an apparent origin at  $\ell_T^+$  below the crest ( $z^+ = -\ell_T^+$ ) that depends on the conditions at the riblet crest plane: no transpiration (figure 4b) or crest transpiration (figure 4c). We discuss the difference between these two conditions in § 3.2. The virtual origin of the mean flow is offset by  $\ell_U^+$  (figure 4a), which is deeper than  $\ell_T^+$  for drag-reducing riblets. As such, the turbulence is effectively pushed away from the wall, which causes the mean flow to slip near the grooves, thereby reducing drag. Luchini (1996) linked these two virtual origins to the drag change  $\Delta U^+$  by noting that the turbulence above riblets does not change relative to a smooth wall, apart from a shift of  $\ell_T^+$ . If true, the relationship between  $\Delta U^+$  and  $\ell_U^+$  and  $\ell_T^+$  follows from the stress balance (at large  $Re_{\tau}$ ),  $dU^+/dz^+ = 1 + \overline{u'w'^+}$ , which constrains the riblet and smooth-wall mean gradients ( $dU^+/dz^+$ ) to match when the turbulence profiles ( $\overline{u'w'}$ ) collapse at all wall-normal locations, i.e. are smooth-wall like. Figure 5(a) shows the Reynolds shear stress profile ( $-\overline{u'w'^+}$ ) against the wall-normal distance from the riblet crest,  $z^+$ . Here, we see a scatter in  $-\overline{u'w'^+}$  between riblet shapes and sizes. In figure 5(b), however, the same data are now shifted by their respective  $\ell_T^+$  in the wall-normal direction, which collapses with the smooth-wall profile, consistent with Luchini (1996). We compute  $\ell_T^+$  by the wall-normal shift that optimally collapses with the smooth-wall Reynolds stress profile at heights in the range  $4 \lesssim z^+ \lesssim 6$ . We also find that the energy distribution across scales of near-wall turbulence over riblets mimics that above a smooth wall. Figure 6

shows the premultiplied two-dimensional cospectra of Reynolds shear stress at matched height above the virtual origin of turbulence of riblets ( $z^+ + \ell_T^+ \approx 5$ ) compared with that of a smooth wall. Here, we observe a general trend that the near-wall turbulent structures are smooth-wall like for riblet sizes below the optimal ( $\ell_g^+ \lesssim 10$ ). The smooth-wall-like behaviour above riblets suggests that quasi-streamwise vortices are maintained without a change in their statistics above the small grooves, except that they perceive an apparent origin at  $z^+ = -\ell_T^+$  (Gómez-de-Segura *et al.* 2018a). Now, in figure 4(a), if we set the origin of the smooth-wall mean profile at  $z^+ = -\ell_T^+$ , then the difference between the origins of the smooth and riblet mean velocity profiles is  $\ell_U^+ - \ell_T^+$ . And since there is a unity (viscous-scaled) mean velocity gradient near the wall, the difference in mean velocity approaching the crest is also  $U^+ - U_0^+ = \ell_U^+ - \ell_T^+$ , where  $U_0^+$  is the mean velocity above the smooth wall. Then from the stress balance, since  $\overline{u'w'^+}$  profiles collapse, the gradient  $dU^+/dz^+$  is the same at every  $z^+ + \ell_T^+$  above the crest, and therefore, the velocity difference near the crest propagates into the overlying flow (Luchini 1996). This gives

$$-\Delta U^+ \approx \ell_U^+ - \ell_T^+ = (\ell_U/\ell_g - \ell_T/\ell_g)\ell_g^+, \quad (3.2)$$

which we observe to be valid for riblets below the optimal size  $\ell_g^+ < 10.7$ . Figure 5(c) shows the scatter between riblet shape and sizes in the mean velocity profiles along  $z^+$ . In figure 5(d), the mean velocity profiles as a function of the turbulence virtual-origin height,  $z^+ + \ell_T^+$ , now collapse when shifted downwards by their respective  $\ell_U^+ - \ell_T^+$ , thus validating (3.2). We also illustrate (3.2) in figure 3(b) to contrast with (3.1) in figure 3(a). From figure 3(b) we observe that there is still a scatter near the optimal size for (3.2) due to an onset of departure from smooth-wall-like flows, but this scatter is smaller than that of (3.1) shown in figure 3(a). Furthermore, we observe that the linearity between  $\Delta U^+$  and  $\ell_g^+$  near the optimum is preserved for (3.2).

The ansatz of Luchini (1996) suggests that the streamwise and spanwise protrusion heights are identical to the virtual origins of the mean and turbulence, i.e.  $\ell_U^+ = h_{\parallel}^+$  and  $\ell_T^+ = h_{\perp}^+$ , recovering (3.1) with  $\mu_0 = 1$ . Figure 7(a) demonstrates that  $\ell_U^+ = h_{\parallel}^+$  is corroborated by the present data by observing that the ratio  $\ell_U^+/h_{\parallel}^+ \approx 1$ , even for sizes larger than the optimal ( $\ell_g^+ \lesssim 15$ ). However, for the turbulence virtual origin,  $\ell_T^+ \neq h_{\perp}^+$ , even for riblet sizes near the optimum  $5 \lesssim \ell_g^+ < 10.7$  (figure 7b). The turbulence virtual origins  $\ell_T^+$  are generally deeper than  $h_{\perp}^+$  ( $\ell_T^+/h_{\perp}^+ > 1$ ), but seem to asymptote to  $h_{\perp}^+$  towards vanishingly small sizes ( $\ell_g^+ \rightarrow 0$ ), consistent with Luchini *et al.* (1991). We also observe that  $\ell_T^+$  deviates less from  $h_{\perp}^+$  for riblets with narrower (higher height-to-spacing ratio) grooves (e.g. M M M M) for sizes below the optimal ( $\ell_g^+ \lesssim 10.7$ ). For the post-optimal riblet sizes ( $\ell_g^+ \gtrsim 10.7$ ), a much larger deviation from  $h_{\perp}^+$  is observed. Note that the value of  $\ell_T^+$  for these post-optimal riblets does not accurately represent the turbulence virtual origin. When attempting to collapse the Reynolds stress profile in the range  $4 \lesssim z^+ \lesssim 6$  (to find  $\ell_T^+$ ), the virtual origin of the Reynolds stress is not well defined due to the departure from smooth-wall-like turbulence. For pre-optimal riblets, however, the virtual origin of the Reynolds stress profile is the same as the smooth wall when shifted by  $\ell_T^+$ , as observed in figure 5(b). Within these pre-optimal riblet sizes, we seek an accurate (viscous) drag model capable of predicting  $\ell_T^+$  for all riblet shapes. One reason  $\ell_T^+ > h_{\perp}^+$  is because the calculation of  $h_{\perp}^+$  neglects transpiration at the riblet crest plane (Gómez-de-Segura *et al.* 2018a). Here, transpiration refers to the spanwise-varying wall-normal flow in the

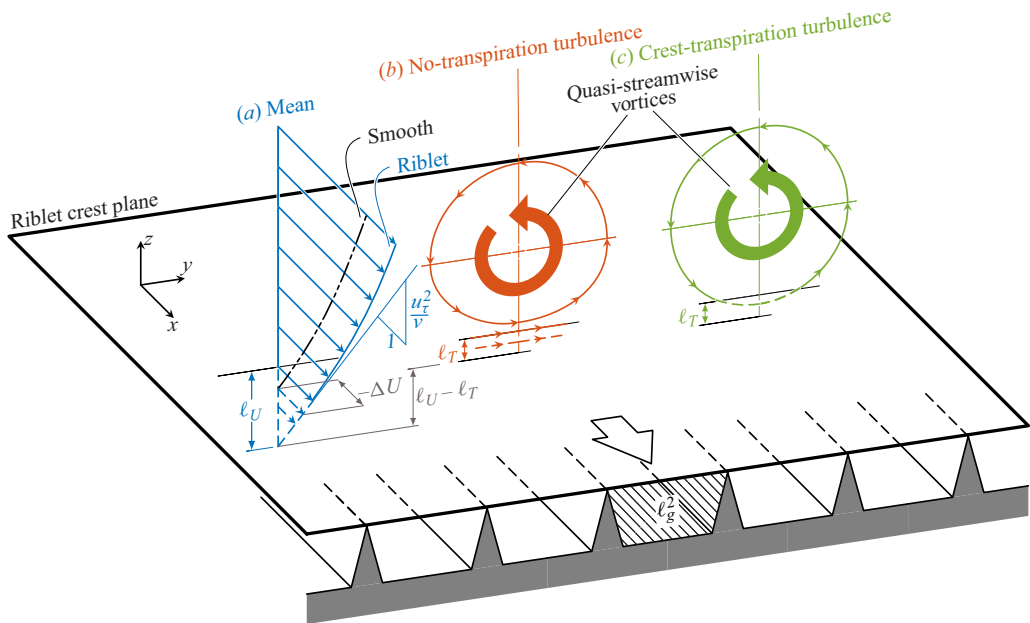


Figure 4. Small (viscous-scaled) riblets offset the apparent origins of the mean and turbulent flows downwards by (a)  $\ell_U$  and (b,c)  $\ell_T$ , respectively, relative to the riblet crests ( $z = 0$ ). The turbulence (quasi-streamwise vortices) does not change relative to a smooth wall, apart from the  $\ell_T$  offset (Luchini 1996). The difference between the offsets quantifies the drag reduction,  $-\Delta U^+ \approx \ell_U^+ - \ell_T^+$  (Luchini 1996; García-Mayoral *et al.* 2019). (b) Luchini *et al.* (1991) suggested that the near-wall turbulence is dominated by spanwise motions, which is valid for vanishingly small riblets. (c) Presently, we include the effects of transpiration at the crest plane, which is crucial in setting  $\ell_T^+$  (Gómez-de-Segura *et al.* 2018a; Ibrahim *et al.* 2021) for non-vanishing riblets.

cross-plane (predominantly induced by quasi-streamwise vortices), and does not refer to the variations of the streamwise velocity in the streamwise direction (cf. Bottaro 2019). The slip/transpiration simulations of Habibi Khorasani *et al.* (2022), which permit transpiration in both of these senses, show that it is indeed transpiration due to spanwise variation of the spanwise velocity that determines the displacement of quasi-streamwise vortices, and thus to the near-wall turbulent mixing and the generation of Reynolds stresses upon which  $\ell_T^+$  is defined.

### 3.2. Transpiration effects at the riblet crest plane

Gómez-de-Segura *et al.* (2018a) and Ibrahim *et al.* (2021) show that the turbulence virtual origin  $\ell_T^+$  is not set by the virtual origin for the spanwise velocity alone, but that wall-normal velocity (transpiration) also plays a role. They performed textureless DNS channel simulations with a Robin boundary condition prescribed on a reference plane ( $z = 0$ ) for the streamwise ( $u|_{z=0} = \ell_x \partial u / \partial z|_{z=0}$ ), spanwise ( $v|_{z=0} = \ell_y \partial v / \partial z|_{z=0}$ ) and wall-normal ( $w|_{z=0} = \ell_z \partial w / \partial z|_{z=0}$ ) instantaneous velocities, where  $\ell_x$ ,  $\ell_y$  and  $\ell_z$  are prescribed slip/transpiration lengths. These DNSs are termed slip/transpiration simulations. Physically, the streamwise and spanwise slip lengths,  $\ell_x$  and  $\ell_y$ , correspond to the local equivalent distances below the reference plane at which a no-slip boundary condition is satisfied if the flow field is extrapolated linearly below the reference plane (Lauga & Stone 2003). For the wall-normal velocity, however,  $\ell_z$  does not convey a slip effect but provides a local transpiration at the reference plane (Gómez-de-Segura *et al.*

A viscous vortex model for riblet drag reduction predictions

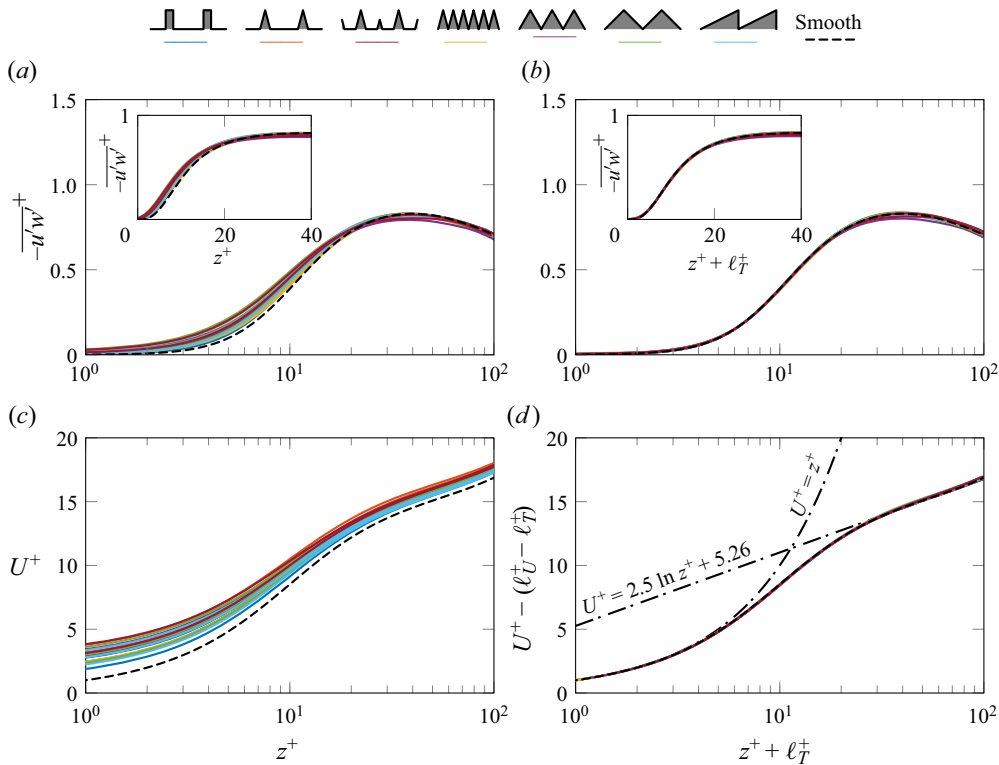


Figure 5. (a,b) Reynolds shear stress for small riblets ( $\ell_g^+ \lesssim 10.7$ ) with (a) the wall-normal coordinate origin at the crest,  $z^+$ , and (b) the wall-normal origin at the turbulence virtual origin,  $z^+ + \ell_T^+$ , which displays a smooth-wall-like behaviour. Inset shows the same profiles with linear-scaled wall-normal coordinate. (c,d) Mean velocity profile for all small riblets ( $\ell_g^+ \lesssim 10$ ) as a function of (c) the crest-origin height,  $z^+$ , and (d) turbulence virtual-origin height,  $z^+ + \ell_T^+$ . The velocity profiles in (d) are shifted downwards by the respective  $\ell_U^+ - \ell_T^+$  that collapse perfectly with the smooth-wall profile ( $\ell_U^+ = \ell_T^+ = 0$ ), hence  $-\Delta U^+ \approx \ell_U^+ - \ell_T^+$  (Gómez-de-Segura *et al.* 2018a; Garcia-Mayoral *et al.* 2019; Ibrahim *et al.* 2021).

2018a). The slip/transpiration simulations of Gómez-de-Segura *et al.* (2018a) and Ibrahim *et al.* (2021) demonstrate that  $\ell_T^+$  does not depend on the prescribed streamwise slip length  $\ell_x^+$ , no matter how large, but only on both  $\ell_y^+$  and  $\ell_z^+$  (cross-flow slip and transpiration lengths). This dependency suggests that  $\ell_T^+$  is the origin perceived by the quasi-streamwise vortices that induce velocities in  $y$  and  $z$  (cf. Habibi Khorasani *et al.* 2022), as first proposed by Luchini *et al.* (1991). The independence to  $\ell_x^+$ , meanwhile, suggests that the origin of the streaks (the streamwise velocity fluctuations) does not influence  $\ell_T^+$  (figure 11 of Ibrahim *et al.* 2021).

From the results of these slip/transpiration simulations, Ibrahim *et al.* (2021) proposed an empirical expression for  $\ell_T^+$  in the smooth-wall-like regime

$$\ell_{T,fit}^+ \approx \begin{cases} \ell_w^+ + \frac{(\ell_v^+ - \ell_w^+)}{1 + (\ell_v^+ - \ell_w^+)/5}, & \text{if } \ell_v^+ > \ell_w^+, \\ \ell_v^+ & \text{if } \ell_v^+ \leq \ell_w^+, \end{cases} \quad (3.3)$$

as a function of the virtual origins of the spanwise and wall-normal root-mean-squared (r.m.s.) velocities,  $\ell_v^+$  and  $\ell_w^+$ , respectively. These virtual origins ( $\ell_v^+$  and  $\ell_w^+$ ) are computed

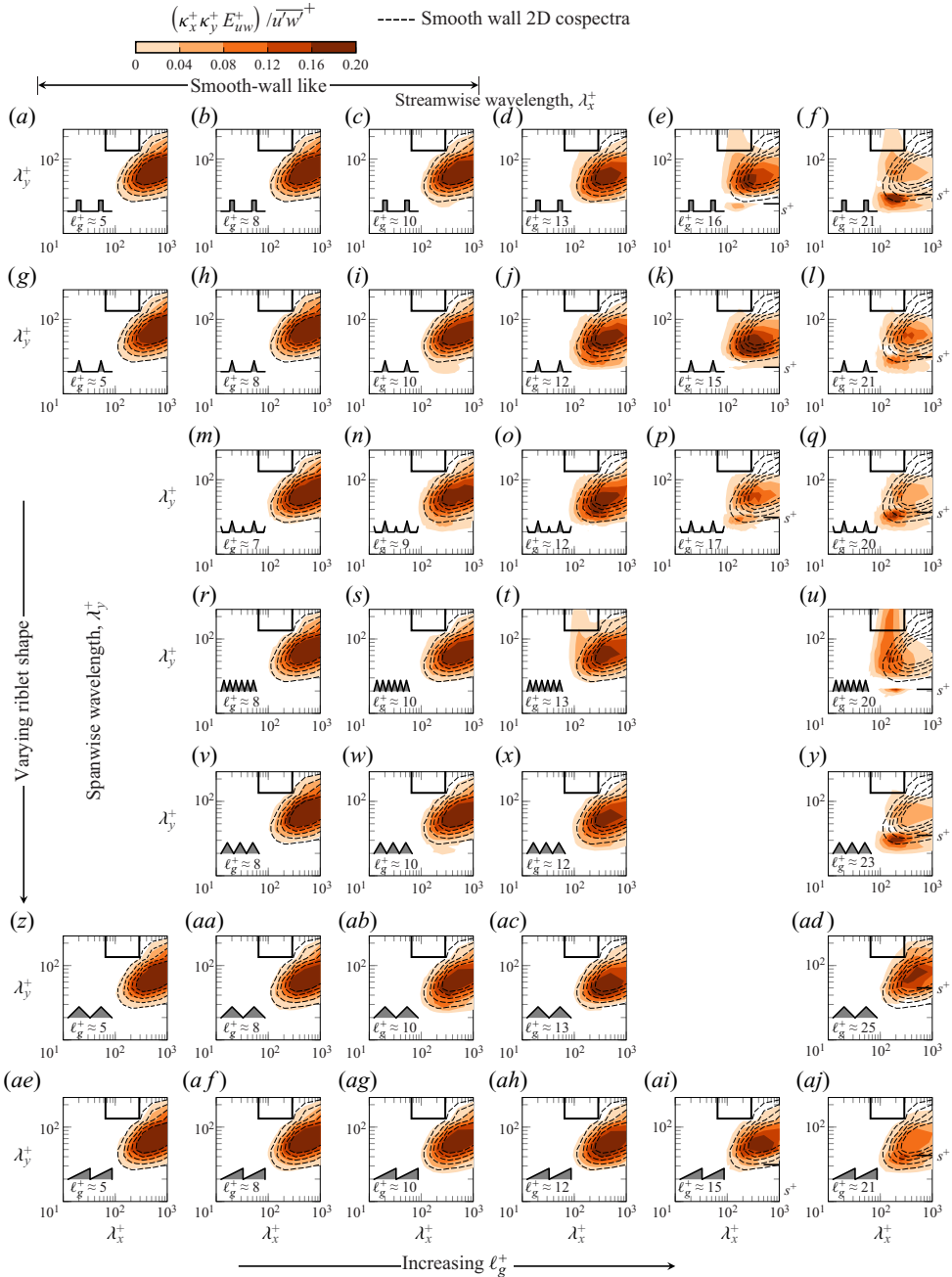


Figure 6. Premultiplied two-dimensional cospectra of Reynolds shear stress,  $\kappa_x^+ \kappa_y^+ E_{uw}^+$ , in the plane,  $z^+ + \ell_g^+ \approx 5$ . The contours are normalised by the matched Reynolds stress at the height of the plane  $\overline{u'w'^+} = \int_0^\infty \int_0^\infty E_{uw}^+ d\lambda_x^+ d\lambda_y^+$ , where  $\lambda_x$  and  $\lambda_y$  are the streamwise and spanwise wavelengths. Contours for smooth walls (---) are compared with contours for riblets (filled). All available  $\ell_g^+ \lesssim 8$  riblets show smooth-wall-like turbulence, whilst the onset of deviation from smooth walls is observed to occur at  $\ell_g^+ \approx 10$ , except for the two-scale trapezoids ( $\blacktriangle\blacktriangle\blacktriangle$ ) at  $\ell_g^+ \approx 7$ . For large riblets ( $\ell_g^+ \gtrsim 20$ ), the co-spectra contours generally break at  $\lambda_y^+ \approx s^+$  (—), which indicates pinning of turbulent structures by the riblet textures. Boxes near the top delimit the region of Kelvin–Helmholtz rollers (García-Mayoral & Jiménez 2011*b*), which are present in  $\blacksquare$  and  $\blacksquare\blacksquare\blacksquare$  (Endrikat *et al.* 2021*a*).



A viscous vortex model for riblet drag reduction predictions

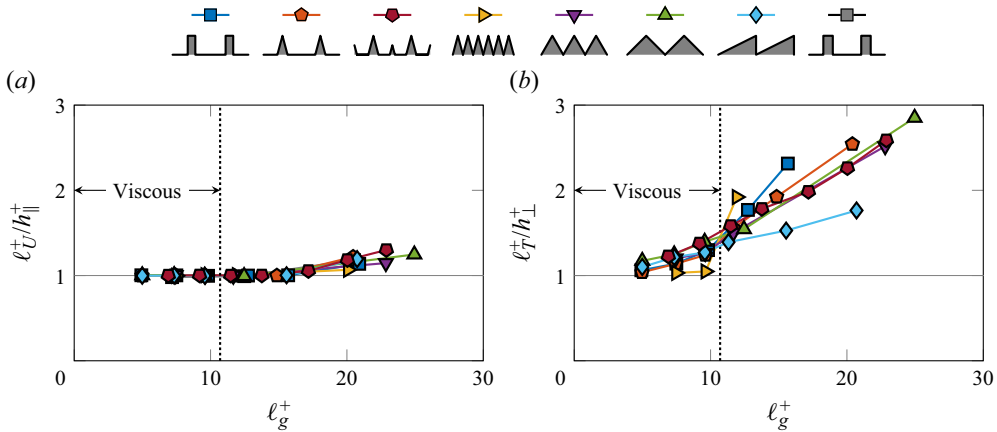


Figure 7. Comparison between (a) the observed mean virtual origin  $\ell_U^+$  from the DNS, and Stokes-flow streamwise protrusion height  $h_{\parallel}^+$  and between (b) the observed turbulent virtual origin from the DNS  $\ell_T^+$ , and Stokes-flow spanwise protrusion height  $h_{\perp}^+$ , for non-vanishing riblet sizes,  $\ell_g^+ \gtrsim 5$ . The mean virtual origin  $\ell_U^+$  is computed by the distance from the crest to the virtual origin of the linearly extrapolated mean velocity profile with a gradient measured locally at  $z^+ \approx 1$ . The turbulence virtual origin  $\ell_T^+$  is computed by the wall-normal shift that best collapses the smooth-wall Reynolds stress profile within heights in the range  $4 \lesssim z^+ \lesssim 6$ .

by collapsing the near-wall r.m.s. profiles from the DNSs with that of the smooth wall, and are related to (but distinct from) the slip/transpiration lengths ( $\ell_y^+$  and  $\ell_z^+$ ). Here, when transpiration is allowed at the boundary-condition plane (non-zero r.m.s. wall-normal velocity, i.e.  $\ell_w^+ \neq 0$ ), the quasi-streamwise vortices are able to penetrate closer to the wall, which deepens the turbulence virtual origin  $\ell_T^+$  (Gómez-de-Segura *et al.* 2018a), as shown by (3.3).

For pre-optimal riblets ( $\ell_g^+ \lesssim 10.7$ ), we presently use (3.3) to explain the relationship between  $\ell_T^+$  and transpiration (i.e.  $\ell_w^+$ ). Figure 8(a) compares the DNS-obtained  $\ell_T^+$  and the empirical  $\ell_{T,fit}^+$ , showing good agreement, except for the two-scale trapezoidal riblets ( $\blacktriangle\blacktriangle\blacktriangle$ ) which exhibit the onset of departure from smooth-wall-like turbulence at  $\ell_g^+ \approx 7$  (figure 6m). Figure 8(b) demonstrates that all the riblet geometries tested here come close to satisfying  $\ell_v^+ \approx \ell_w^+$  and  $\ell_w^+ \neq 0$ , the latter showing that crest-transpiration effects are relevant. As such,  $\ell_T^+ \approx \ell_v^+ \approx \ell_w^+$  according to (3.3). This agreement (that  $\ell_T^+ \approx \ell_v^+ \approx \ell_w^+$ ) is shown graphically in figure 9, where the r.m.s. cross-flow velocity profiles ( $v'^+$  and  $w'^+$ ) of riblets collapse with those of the smooth wall after a wall-normal shift of  $\ell_T^+$  (contrast figure 9a,b). In the case of non-vanishing riblets, the *a priori* spanwise protrusion height  $h_{\perp}^+$  differs from the *a posteriori* spanwise virtual origin  $\ell_v^+$  (and from  $\ell_T^+$ ), as uniform  $v$  and zero  $w$  (which are used to calculate  $h_{\perp}^+$ ) cannot adequately represent the finite length scale  $v$  and  $w$  fluctuations, typical of near-wall streamwise vortices near the crest.

Figures 9(c) and 9(d) show that the r.m.s. streamwise vorticity fluctuation intensities,  $\omega_x'^+$ , for riblets also collapse with the smooth wall when shifted by  $\ell_T^+$  ( $\ell_T^+$  having been determined from the Reynolds shear stress), suggesting a strong correspondence between the streamwise vorticity and Reynolds shear stress. This collapse is also observed in the  $\omega_x'^+$  profiles from slip/transpiration simulations of Gómez-de-Segura & García-Mayoral (2020) when  $\ell_v^+ \approx \ell_w^+$ . For the streamwise r.m.s. profiles  $u'^+$ , a shift of  $\ell_T^+$  do not result in the collapse with the smooth-wall profile (see different peaks at  $z^+ \approx 15$  and slopes at  $z^+ \lesssim 5$  in figure 9b); a similar behaviour was observed in the  $u'^+$  profiles of Ibrahim

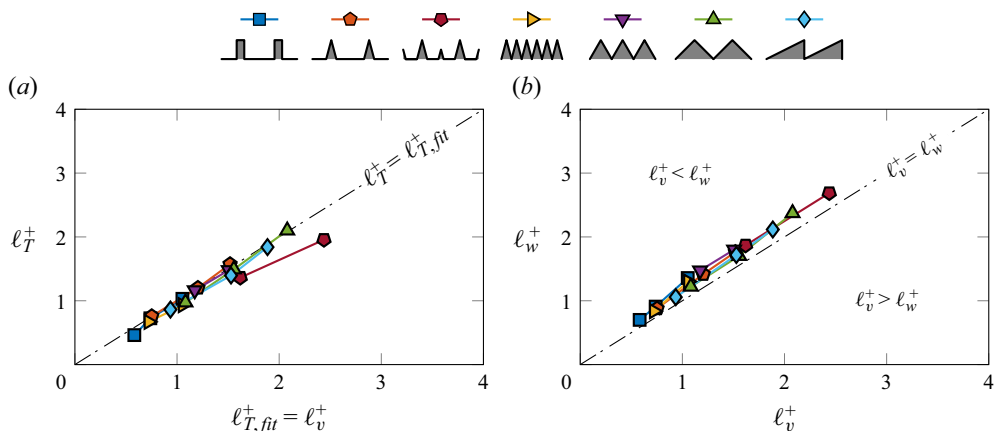


Figure 8. (a) Turbulence virtual origin of riblets,  $l_T^+$  from DNS agree with  $l_{T,fit}^+$  for  $l_g^+ \lesssim 10.7$  with the exception of  $\text{▲▲▲▲}$  riblets due to an onset of non-smooth-wall-like turbulence at  $l_g^+ \approx 7$  in figure 6. (b) Riblets of sizes  $l_g^+ \lesssim 10.7$  are in the  $l_v^+ \approx l_w^+$  regime regardless of shape, and thus, based on the empirical fit (3.3) by Ibrahim *et al.* (2021),  $l_{T,fit}^+ \approx l_v^+ \approx l_w^+$ .

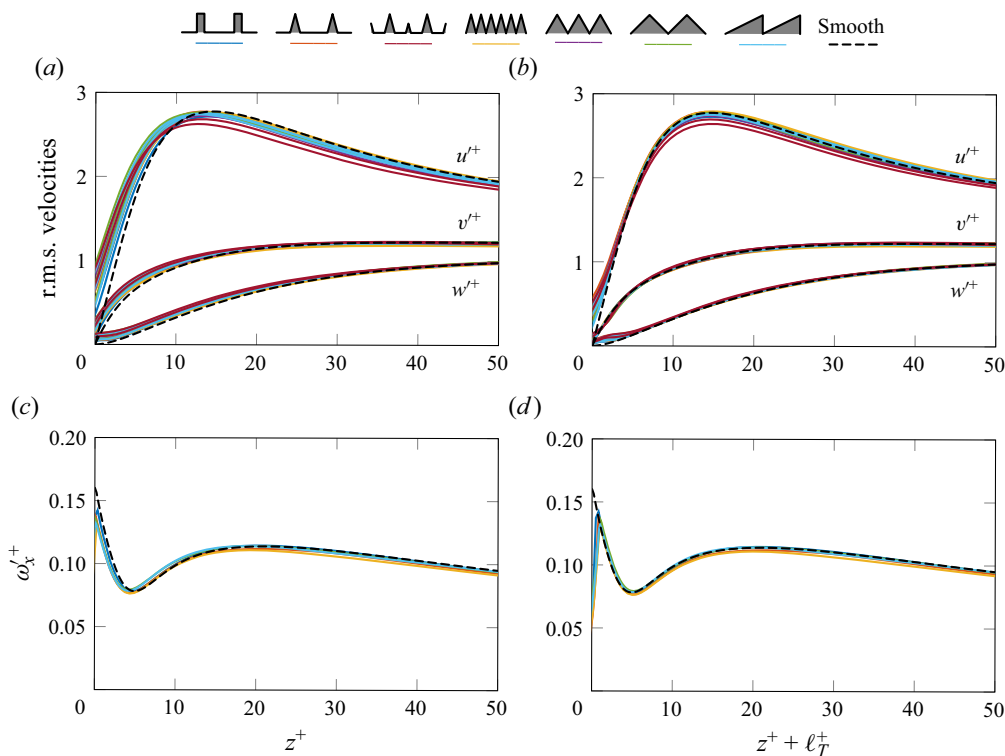


Figure 9. (a,b) Root-mean-squared streamwise ( $u^+$ ), spanwise ( $v^+$ ) and wall-normal ( $w^+$ ) velocity fluctuations and (c,d) streamwise vorticity fluctuation profiles for small riblets ( $l_g^+ \lesssim 10.7$ ) and smooth wall (S395) from table 2 as a function of (a,c)  $z^+$  (crest origin) and (b,d)  $z^+ + l_T^+$  (turbulence virtual origin). The collapse of  $v^+$  and  $w^+$  profiles in (b) further corroborates (3.3), whilst that in (d) is consistent with the profiles from the slip/transpiration simulations of Gómez-de-Segura & García-Mayoral (2020).

*et al.* (2021). This implies that the streamwise fluctuations do not contribute to setting the turbulence virtual origin,  $\ell_T^+$ .

This validation of (3.3) with riblets suggests that  $\ell_T^+$  can be predicted accurately when incorporating crest-transpiration effects. Presently, we propose a model to quantify  $\ell_T^+$  *a priori* by explicitly modelling an effect of the quasi-streamwise vortices near the wall, bypassing the empirical expression to find  $\ell_T^+$ . In doing so, we will be able to form a physically justified model of the non-trivial behaviour of the empirical model (3.3).

### 3.3. Models of quasi-streamwise vortices

Vortical structures that consist of spanwise-varying cross-flow velocities have been previously modelled as a sinusoidal wave with one or a combination of two spanwise wavelengths,  $\lambda_y^+$  (Coles 1978; Chapman & Kuhn 1986; Pollard *et al.* 1994). Pollard *et al.* (1994) proposed a spanwise and time-varying sinusoidal function for the prescribed upper bound streamwise ( $u'$ ), spanwise ( $v'$ ) and wall-normal ( $w'$ ) velocity fluctuations, using two values of  $\lambda_y^+$  to model the autonomous behaviour of turbulence. Using these upper boundary conditions, they numerically solved the Navier–Stokes equations in a two-dimensional height-restricted domain ( $L_z^+ \approx 40$ ) with no-slip smooth or riblet wall at the bottom. This model is similar to that of Chapman & Kuhn (1986), where they also solved the Navier–Stokes equation in a two-dimensional height-restricted domain, but only for a smooth wall (see also Minnick 2022). Both models by Pollard *et al.* (1994) and Chapman & Kuhn (1986) resolve the turbulence profile ( $\overline{u'w'}$ ) for both smooth and riblet walls, which can be used to predict  $\ell_T^+$ . However, these models require a Navier–Stokes simulation (involving the nonlinear terms). Coles (1978) suggested a simpler viscous sublayer model for the turbulence by approximating the velocity fluctuations using a time-independent, sinusoidal function, where the amplitudes are height dependent, tuned using an equation for the mean sublayer profile by Spalding (1961). These velocities are approximated using one mode with a spanwise wavelength of  $\lambda_y^+ = 100$ , following from the typical spanwise spacing between two adjacent near-wall coherent streaks (Kline *et al.* 1967; Smith & Metzler 1983). Using this viscous sublayer model by Coles (1978), a turbulence profile up to  $z^+ \approx 15$  can be obtained. The viscous sublayer model by Coles (1978) is straightforward, but does not provide an extension to riblet walls. The model from Pollard *et al.* (1994) is able to include the riblet wall, but an unsteady numerical simulation of the two-dimensional Navier–Stokes equations is required.

These aforementioned models motivate our present modelling approach in § 4. We briefly discuss the present approach with the aid of an instantaneous wall-normal velocity field in the cross-plane in figure 10. In this region, a single isolated quasi-streamwise vortex induces an ejection event (Robinson 1991), which lifts up a streak, that is spaced approximately 100 viscous units from the neighbouring streak (Kline *et al.* 1967; Smith & Metzler 1983). These quasi-streamwise vortices are invariant across the outer-flow geometry and Reynolds number (Schlatter *et al.* 2014). Each vortex has an average diameter of  $d^+ \approx 20$ –40 (Kim, Moin & Moser 1987; Robinson 1991) and is essentially streamwise aligned with a length of 300 viscous units (Jeong *et al.* 1997). The cores of these vortices are, on average, located 20 viscous units above a smooth wall (Kim *et al.* 1987). This average is based on the location of the local peak in the r.m.s. streamwise vorticity profile (figure 9*c,d*).

The scales of the quasi-streamwise vortices inform the region of interest for the present model. Here, we employ a two-dimensional domain with a smooth or riblet wall at the bottom, following Pollard *et al.* (1994), but we solve the (viscous) Stokes equations,

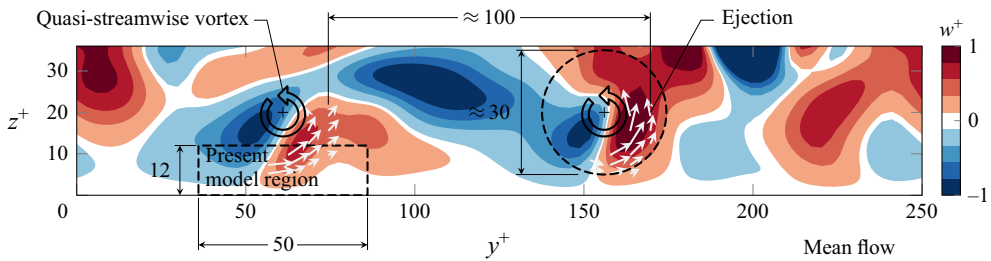


Figure 10. Instantaneous wall-normal velocity field in the  $yz$ -plane of the smooth-wall minimal-channel case (S395). Mean flow is out of the page. Near the wall ( $10 \lesssim z^+ \lesssim 20$ ), the intense wall-normal-velocity regions (dark blue and dark red) are induced by quasi-streamwise vortices (circular arrows). Grey arrows indicate the cross-flow velocity field, where ejection events (which lift up streaks) can be identified and observed to have a spacing of about 100 viscous units in the span (Kline *et al.* 1967; Smith & Metzler 1983). On average, the core diameter of these vortices are 30 viscous units (dashed circular region of intense streamwise vorticity) with the centre ('+' symbols) located 20 viscous units above the wall. The dashed rectangular area represents the region of interest for the viscous vortex model, where the upper boundary is exposed to an overlying vortex that induces wall-normal (transpiration) and spanwise fluctuations.

further restricting the domain height to the near-wall region,  $z^+ \approx 12$  (see shaded region, figure 10). Since the  $\ell_T^+$  shift is near the riblet wall, we do not need an explicit model for quasi-streamwise vortices (including their autonomous behaviour) farther away from the riblet wall. Instead, restricting the domain height to the near-wall region allows us to model the viscous response below these vortices. As such, the boundary condition at  $z^+ \approx 12$  of our present model is an ensemble-averaged flow induced by quasi-streamwise vortices, characterised by spanwise and wall-normal velocities varying sinusoidally in the spanwise direction and modelled using a single wavelength,  $\lambda_y^+$ , similar to Coles (1978). Jiménez, del Álamo & Flores (2004) noted that the spanwise wavelength of a vortex is  $\lambda_y^+ \approx 50$ , as they observed the peak in the wall-normal velocity spectral density at  $\lambda_y^+ \approx 50$  and  $\lambda_x^+ \approx 300$ , aligning closely with the signature of a quasi-streamwise vortex (Kim *et al.* 1987; Robinson 1991; Jeong *et al.* 1997; Schlatter *et al.* 2014). In Appendix B, we perform a parameter calibration and sensitivity study to further inform our choice of  $\lambda_y^+ = 50$ . We further show in § 4 that a single  $\lambda_y^+$  from the full turbulent flow signal is sufficient to determine  $\ell_T^+$ . We neglect the streamwise velocity  $u$  because it is not responsible in setting  $\ell_T^+$  (Ibrahim *et al.* 2021). Since  $u$  is absent, the present model does not provide a turbulence profile  $\overline{u'w'}$ . Instead, we calculate  $\ell_T^+$  from the model by collapsing the r.m.s. streamwise vorticity profiles with a smooth-wall reference case. Indeed, the r.m.s. vorticity profiles also shift with the turbulence above riblets as shown in figure 9(d).

The spirit of the model is similar to the stretched spiral vortex by Lundgren (1982), where a simple flow structure allows us to calculate properties of the turbulent flow (cf. Pullin & Saffman 1993). In our present model, we allow a simple vortical structure to interact with non-vanishing riblet textures in order to yield  $\ell_T^+$ . The present approach departs from homogenisation techniques, which require the texture sizes to be vanishingly small compared with the turbulent scales. It also bypasses resolving the autonomous, nonlinear behaviour of turbulence over riblets (Pollard *et al.* 1994; Minnick 2022), by predicting an averaged near-wall response induced by a quasi-streamwise vortex.

#### 4. The viscous vortex model

The present model, which we term the viscous vortex model, predicts  $\ell_T^+$  by modelling the averaged near-wall response below a quasi-streamwise vortex governed by the steady, two-dimensional Stokes equations. The key aspect of the viscous vortex model, in contrast to the homogenisation approaches of Luchini *et al.* (1991) and Bottaro (2019), is that it does not require scale separation between turbulent flow structures and riblet textures. The model is designed to be applicable for non-vanishing, optimal riblet sizes where turbulent flow structures and riblet textures are comparable. We further demonstrate that the viscous vortex model is calibrated by smooth-wall DNS data alone, as we observe from the DNSs that the unpinned, smooth-wall-like nature of quasi-streamwise vortices persists even above riblet surfaces (see § 4.3). This observation suggests that the influence of riblets on the behaviour of these vortices is relatively limited, and the viscous vortex model remains applicable even in the presence of riblets up to the optimal size.

##### 4.1. Formulation and methodology

This section includes a brief overview of the formulation and methodology of the viscous vortex model. We discuss further details of the model in §§ 4.2–4.3.

Figure 11 shows the viscous vortex domain used to model the flow below a quasi-streamwise vortex (representing turbulence). Here, we model a two-dimensional flow in the cross ( $yz$ ) plane, i.e.  $\partial/\partial x = 0$ , given that the quasi-streamwise vortices are relatively long,  $\approx 300$  (Jeong *et al.* 1997; Schlatter *et al.* 2014) compared with the optimal riblet spacing ( $s^+ \approx 15$ , table 2). The model is an ensemble-averaged flow structure below a quasi-streamwise vortex (figure 10). The strength of this averaged structure is obtained by averaging the cross-flow Fourier amplitudes from smooth-wall DNSs (see § 4.2). Nonlinearity is essential in setting the strength of the near-wall structures (streaks and vortices) of the autonomous self-sustaining process in the buffer region  $10 \lesssim z^+ \lesssim 30$  (e.g. Jiménez 2018). However, by modelling only the flow very near the wall below the self-sustaining process in the buffer layer, we bypass directly contending with the nonlinearity. Instead, we only use a product of this nonlinear process, namely the strength of the vortical structures, as model input, which we measure once in a smooth-wall simulation since this part is identical to that of small riblets (e.g. figure 6). Thus, the modelled flow is governed by the steady Stokes equations

$$-\frac{1}{\rho} \frac{\partial p}{\partial y} + \nu \left( \frac{\partial^2 v}{\partial y^2} + \frac{\partial^2 v}{\partial z^2} \right) = 0, \quad -\frac{1}{\rho} \frac{\partial p}{\partial z} + \nu \left( \frac{\partial^2 w}{\partial y^2} + \frac{\partial^2 w}{\partial z^2} \right) = 0, \quad \frac{\partial v}{\partial y} + \frac{\partial w}{\partial z} = 0, \quad (4.1a-c)$$

which are derived by neglecting nonlinearity and ensemble averaging the  $y$  and  $z$  components of (2.1). We neglect the  $x$  component of (2.1) because  $\ell_T^+$  only depends on the cross-flow velocities (Ibrahim *et al.* 2021). Up to here, this is the same set-up as that for calculating  $h_{\perp}^+$  (Luchini *et al.* 1991), that is meant to be  $\ell_T^+$ . However, instead of prescribing spanwise-homogeneous, or infinitely large scale velocities at the top (Luchini *et al.* 1991), we will instead prescribe the top velocities with a given scale (wavelength) and intensities (amplitudes)

$$w(y, z = h) = -A \sin(\beta y), \quad v(y, z = h) = -B \sin(\beta y + \Phi), \quad (4.2a,b)$$

as illustrated at the top of figure 11. Here,  $A$  and  $B$  are the prescribed amplitudes,  $\Phi$  is the prescribed phase difference,  $h$  is the prescribed height of the model domain measured from the riblet crest and  $\beta$  is the period that is related to the prescribed wavelength,

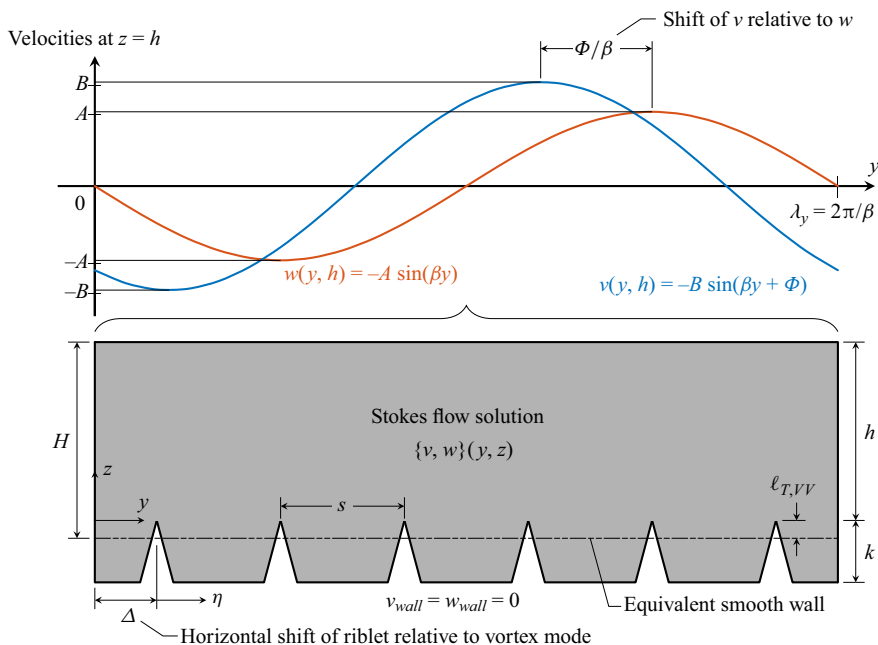


Figure 11. The viscous vortex model. Stokes flow (4.1) is solved in the grey-coloured two-dimensional domain with the given spanwise and wall-normal velocity boundary condition at the top ( $z = h$ ), periodic sides and a no-slip smooth or riblet wall at the bottom. For the riblet surface, a uniform average of the solutions between  $\Delta = 0$  and  $\Delta = s$  along the coordinate  $\eta = y + \Delta$  is performed to incorporate the unpinning, smooth-wall-like character of quasi-streamwise vortices. The model turbulence virtual origin,  $\ell_{T,VV}$ , is measured by the negative offset of the height of the domain  $h$  measured from the crest plane such that the r.m.s. streamwise vorticity matches with that of the equivalent smooth wall at the local minimum (i.e.  $z^+ + \ell_{T,VV}^+ \approx 5$ ).

$\lambda_y$  ( $\beta = 2\pi/\lambda_y$ ). The top boundary condition (4.2) models the action below a vortex in the cross-plane, similar to the formulation of the sublayer model by Coles (1978). Furthermore, transpiration effects at the crest are readily incorporated through (4.2a), which is crucial to accurately predicting  $\ell_T^+$  (Ibrahim *et al.* 2021). Using the modelled cross-flow velocities at the upper boundary (4.2) and a no-slip smooth or riblet wall at the bottom, as well as periodic boundary conditions in the span, we can solve for  $v$  and  $w$  using (4.1).

Even though the Stokes equation (4.1) is formally in the limit of zero Reynolds number, we retain the effect of finite friction Reynolds number,  $Re_\tau$ , in the Stokes calculation through, for example, the riblet spacing,  $s^+$

$$s^+ = \lambda_y^+ (s/\lambda_y)_{VV}, \tag{4.3}$$

where  $\lambda_y^+$  is associated with the quasi-streamwise vortex, and the ratio of riblet size to the wavelength,  $(s/\lambda_y)_{VV}$ , is prescribed in the Stokes calculation. Through this ratio,  $(s/\lambda_y)_{VV}$ , the model captures the non-vanishing riblet sizes relative to the near-wall turbulence (represented by the averaged quasi-streamwise vortex), with the latter characterised by a given universal scale,  $\lambda_y^+$ . From here on, sizes represented in the viscous vortex model are quantified in viscous units (+), using a similar calculation as per (4.3).

The prescribed parameters ( $A$ ,  $B$  and  $\Phi$ ) in (4.2) are obtained through a Fourier analysis of the DNS cross-flow velocities for a smooth and riblet wall, which we outline in detail in § 4.2. As the turbulence above small ( $\ell_g^+ \lesssim 10.7$ ) riblets remains smooth-wall like, we



use the same  $A$ ,  $B$  and  $\Phi$  to model the flow above both smooth and riblet walls. These parameters vary with height above the wall,  $z^+$ , and wavelength,  $\lambda_y^+$ . Once a height and wavelength are chosen, these set the height and span of the model domain, respectively (figure 11). The domain height should be within  $10 \lesssim H^+ \lesssim 15$  such that the modelled flow is below the average height of the vortex centres (Kim *et al.* 1987). This height also provides enough room for the flow to recover from the riblet wall boundary condition. The domain span is restricted by positive-integer ( $n$ ) multiples of  $\lambda_y^+$ , i.e.  $L_y^+ = n\lambda_y^+$ , to ensure the spanwise periodicity of the top boundary condition (4.2).

Next, we specify the spanwise location of the riblet textures relative to the quasi-streamwise vortex, measured by  $\Delta$ , illustrated at the bottom of figure 11. As we will show from the DNS in § 4.3, the quasi-streamwise vortices above smooth-wall-like riblets ( $\ell_g^+ \lesssim 10$ ) have an equal probability of residing at any spanwise location above the riblet wall, which indicates that these vortices are unpinned, like those above a smooth wall. We model this unpinned character of these vortices by a uniform average of the Stokes field across spanwise shifts of the riblet wall in the range  $0 \leq \Delta \leq s$ .

Using the above procedure, the modelled flow fields above smooth and riblet walls can be obtained. These flow fields are used to calculate  $\ell_{T,VV}^+$ , which is the turbulence virtual origin predicted by the viscous vortex model. Here,  $\ell_{T,VV}^+$  is found by iterating the negative offset of the riblet domain height  $h^+$  measured from the crest plane, such that the modelled r.m.s. streamwise vorticity profile,  $\omega'_x$ , matches with that of the equivalent smooth wall at the local minimum (i.e.  $z^+ + \ell_{T,VV}^+ \approx 5$ ). As we will show in § 4.3, once  $\omega'_x$  at the local minimum is matched, the entire profile above the riblet crests ( $z^+ > 0$ ) collapses with the equivalent modelled smooth wall profile. This is analogous to the collapse of the r.m.s. vorticity profiles measured from DNSs of riblet and smooth wall, as shown in figure 9(d), which reinforces that the modelled turbulence above riblets remains smooth-wall like. The output of the viscous vortex model,  $\ell_{T,VV}^+$ , for a range of riblet shape and sizes are reported and compared with  $\ell_T^+$  measured from DNS in § 4.4.

#### 4.2. Smooth-wall-like turbulence

This section outlines the process to obtain the magnitudes of  $A$ ,  $B$  and  $\Phi$  in (4.2), through a Fourier analysis of the DNS cross-flow velocities for smooth and riblet walls. We also show that the DNSs of riblets are not required for the present model because  $A$ ,  $B$  and  $\Phi$  are the same as that for smooth walls at matched height above the turbulence virtual origin.

Figure 12 illustrates the process to obtain samples of the Fourier coefficients of the wall-normal velocity from the minimal-channel smooth-wall DNS (S395). We perform the same analysis for the spanwise velocity. Here, the goal is to extract the parameters for a single spatially localised near-wall quasi-streamwise vortex using a windowed Fourier analysis. At each cross-plane (at fixed  $x$  and  $t$ ), we divide the spanwise and wall-normal ( $v$ ,  $w$ ) velocity fields into overlapping segments of spanwise length,  $L_{ys}^+ \approx 150$ . Figure 12(a) shows a segment for  $0 \lesssim y^+ \lesssim 150$ , in which a vortex can be identified at  $y^+ \approx 60$ . We also take segments at spanwise increments of 50 units,  $50 \lesssim y^+ \lesssim 200$  and  $100 \lesssim y^+ \lesssim 250$  (both are not shown in figure 12a) to ensure we capture a vortex at the centre of the segment. For cases where the DNS channel spans are wider (i.e. SF395 and S1000 in table 2), the fields are segmented with the same  $L_{ys}^+ \approx 150$  and spanwise increments, resulting in more segments per  $yz$ -field. Segmenting the cross-plane is crucial as these vortices are usually isolated in the cross-plane (Robinson 1991; Jiménez

*et al.* 2004; Jiménez 2018). The Fourier amplitudes from unwrapped samples contain distortions resulting from the average effect of multiple vortices (figure 10). The difference between the Fourier amplitudes obtained from segmented and unsegmented signals is discussed in detail in Appendix B.2. In figure 12(b), we multiply each segmented field by the normalised Hann window function,  $\Omega(y^+) = (2/3)^{1/2}[1 - \cos(2\pi y^+/L_{ys}^+)]$ , so that the fields are periodic in  $y$ , and we can take the discrete Fourier transform at each height  $z^+$

$$\{\hat{v}^+, \hat{w}^+\}(\lambda_{y,m}^+ = 2\pi/\kappa_m^+, z^+) = \frac{1}{N_{ys}} \sum_{n=0}^{N_{ys}-1} [\{v_n^+, w_n^+\}(y_n^+, z^+) \Omega(y_n^+)] \exp(-iy_n^+ \kappa_m^+), \quad (4.4)$$

where  $\kappa_m = 2\pi m/L_{ys}$ ,  $y_n = nL_{ys}/N_{ys}$  and  $N_{ys}$  is the number of spanwise discrete points at a fixed height in a segment. In physical space, the velocities for each positive and finite wavelength  $\lambda_y^+ \equiv 2\pi/\beta^+$  can be written in terms of the Fourier coefficients as

$$\{v_{\lambda_y^+}^+, w_{\lambda_y^+}^+\}(y^+, z^+) = 2 \{|\hat{v}^+|, |\hat{w}^+|\} \sin(\beta^+ y^+ + \angle\{\hat{v}^+, \hat{w}^+\} + \pi/2), \quad (4.5)$$

for a fixed height  $z^+$  and for each segment, where  $|\hat{\cdot}| \equiv [\text{Re}\{\hat{\cdot}\}^2 + \text{Im}\{\hat{\cdot}\}^2]^{1/2}$  and  $\angle(\hat{\cdot})$  is the argument of  $(\hat{\cdot})$  from the positive  $\lambda_y^+$ . The factor of 2 in (4.5) is included in the amplitude to combine both positive and negative  $\lambda_y^+$ . We illustrate (4.5) in figure 12(c) for a single  $\lambda_y^+ \approx 50$ , extracted from the full flow field in figure 12(b). We shift the spanwise coordinate  $y^+ = \tilde{y}^+ - (\angle\hat{w}^+ + \pi/2)/\beta^+$  so that these sinusoids resemble the upper boundary velocities of the viscous vortex model in (4.2)

$$w_{\lambda_y^+}^+(\tilde{y}^+, z^+) = 2|\hat{w}^+| \sin(\beta^+ \tilde{y}^+), \quad v_{\lambda_y^+}^+(\tilde{y}^+, z^+) = 2|\hat{v}^+| \sin(\beta^+ \tilde{y}^+ + \angle\hat{v}^+ - \angle\hat{w}^+). \quad (4.6a,b)$$

We extract each component of the signal, namely the amplitude ( $a_j, b_j$ ) and phase difference ( $\varphi_j$ ), given by

$$b_j(\lambda_y^+, z^+) \equiv 2|\hat{v}^+|, \quad a_j(\lambda_y^+, z^+) \equiv 2|\hat{w}^+|, \quad \varphi_j(\lambda_y^+, z^+) \equiv \angle\hat{v} - \angle\hat{w}, \quad (4.7a,b)$$

where  $j$  is the sample index within the range  $1 \leq j \leq N_{seg} N_x N_t$ . The upper bound (maximum number of samples) of  $j$  is the product of the number of segments for each  $yz$ -field ( $N_{seg}$ ), the number of  $yz$ -fields in the streamwise direction ( $N_x$ ) and the number of time snapshots ( $N_t$ ).

Figures 13(a)–13(c) depict the p.d.f. of the samples (4.7) obtained from the smooth-wall DNS cases. These include the full-channel and minimal-channel smooth walls at  $Re_\tau = 395$ , as well as a minimal-channel smooth-wall case at  $Re_\tau = 1000$ . The samples in these p.d.f.s correspond to a height of  $z^+ \approx 12$ , i.e. below the average vortex core height of  $z^+ \approx 20$  (Kim *et al.* 1987) and a sinusoidal wavelength of  $\lambda_y^+ \approx 50$  to represent a quasi-streamwise vortex (Jiménez *et al.* 2004). At this specific height and wavelength, the p.d.f.s for the smooth-wall DNS cases collapse, indicating that the variables  $A$ ,  $B$  and  $\Phi$  are independent of the channel span and friction Reynolds number  $Re_\tau$ . By averaging the amplitude and phase difference across all samples  $j$ , we obtain  $A = 0.2$ ,  $B = 0.28$  and  $\Phi = 0.31\pi$ . A value  $\Phi < 0.5\pi$  indicates that, on average, the quasi-streamwise vortices are tilted with respect to the streamwise direction (cf. Jeong *et al.* 1997; Schlatter *et al.* 2014). Our modelling choices of  $z^+ = 12$  and  $\lambda_y^+ = 50$  (and corresponding values of  $A$ ,  $B$

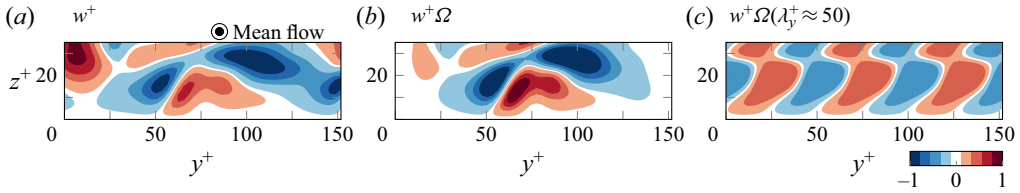


Figure 12. Illustration of the process to extract the Fourier coefficients from both spanwise and wall-normal instantaneous velocities in the cross-plane. Mean flow is out of the page. Instantaneous wall-normal velocity field in the  $yz$ -plane in figure 10 is segmented into overlapping segments of length,  $L_{ys}^+ \approx 150$ :  $0 \lesssim y^+ \lesssim 150$  (shown in *a*),  $50 \lesssim y^+ \lesssim 200$  and  $100 \lesssim y^+ \lesssim 250$  (the last two not shown in the figure). *b*) Segments are multiplied by a normalised Hann window function,  $\Omega(y^+) = (2/3)^{1/2} [1 - \cos(2\pi y^+/L_{ys}^+)]$  so that a Fourier transform can be applied. *c*) Resulting field for one wavelength,  $\lambda_y^+ \approx 50$ , where samples of the Fourier amplitudes as a function of  $z^+$  can be obtained.

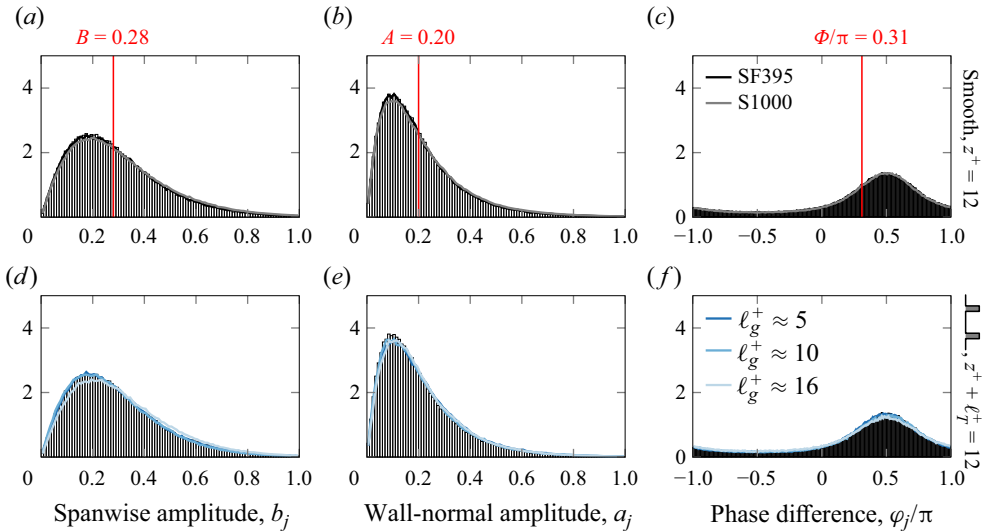


Figure 13. Probability density functions (p.d.f.s) of the cross-flow parameters extracted from DNS (4.7a,b). These parameters correspond to  $\lambda_y^+ \approx 50$  at a height of  $z^+ + \ell_T^+ \approx 12$ . The p.d.f.s of the smooth-wall minimal-channel case at  $Re_\tau = 395$  are represented by the vertical bars in *(a-f)*, compared with *(a-c)* the full-channel  $Re_\tau = 395$  smooth-wall case (—) and the minimal-channel  $Re_\tau = 1000$  smooth-wall case (—, grey), as well as *(d-f)* the blade (▬) riblet cases with  $\ell_g^+ \approx 5, 10$  and  $16$  (dark blue to light blue). The red vertical lines represent the mean values of these sample p.d.f.s, which are prescribed in the viscous vortex model, along with  $\lambda_y^+ = 50$  and  $H^+ = 12$ .

and  $\Phi$ ) are additionally supported by a parameter calibration and sensitivity study outlined in Appendix B.

As demonstrated in figures 13(d)–13(f), the values of  $A$ ,  $B$  and  $\Phi$  obtained from minimal-channel DNSs of blade riblets (▬) with sizes of  $\ell_g^+ \lesssim 10$  (i.e. cases BL08 and BL16 from table 2) are consistent with those from smooth-wall DNSs. For these riblets ( $\ell_g^+ < 10$ ), the p.d.f.s collapse when the parameters are extracted at equivalent heights above the turbulence virtual origin,  $z^+ + \ell_T^+ \approx 12$ . This collapse further shows that the turbulence above riblets behaves like that above a smooth wall, and demonstrates that only smooth-wall DNS data are required to obtain  $A$ ,  $B$  and  $\Phi$ . The p.d.f.s for

large, non-smooth-wall-like riblets ( $\ell_g^+ \approx 16$ ) in figures 13(d)–13(f) appear similar to the smooth-wall equivalents, but exhibit noticeably lower peaks in  $b_j$  and  $\varphi_j$ , suggesting that  $A$ ,  $B$ , and  $\Phi$  at  $\lambda_y^+ \approx 50$  and  $z^+ + \ell_T^+ \approx 12$  are not overly sensitive to the drag-increasing mechanisms associated with these riblets, in contrast to the full Reynolds stress cospectra at  $z^+ + \ell_T^+ \approx 5$  (figure 6e).

The above observation suggests that the information from one wavelength is sufficient to compute  $\ell_T^+$ . Moreover, this wavelength ( $\lambda_y^+ = 50$ ) is also of the same order as the riblet sizes ( $10 \lesssim s^+ \lesssim 15$ ). Thus, these parameters for obtaining  $\ell_T^+$  appear robust and do not require the stricter scale separation between the riblet textures and turbulence imposed on homogenisation techniques.

### 4.3. The unpinned, smooth-wall-like quasi-streamwise vortices above riblets

In this section, we justify from DNS that the quasi-streamwise vortices above riblets are unpinned like those above a smooth wall. We incorporate this character of vortices in the viscous vortex model by a uniform average of the solutions across spanwise shifts  $\Delta$  of the riblet texture (figure 11).

We have previously shown, from the DNSs, that the flow above small riblets ( $\ell_g^+ \lesssim 10.7$ ) is smooth-wall like in terms of the collapse of the Reynolds stress profiles (figure 5b) and the collapse of Fourier amplitudes and phases (figures 6 and 13). Thus, we expect the quasi-streamwise vortices (representing turbulence) above riblet walls to behave as if above featureless smooth walls, which have no preferential spanwise position relative to the riblets. Figure 14 shows that these vortices above either a smooth wall or small riblets are unpinned, through a uniform p.d.f. of the DNS cross-flow velocity phase shifts at wavelengths  $\lambda_y^+$  similar to the average diameter of a vortex. Here, we quantify the relative spanwise positions of the vortex by phase shifts of the spanwise and wall-normal velocities,  $\phi_v \equiv \angle \hat{v}$  and  $\phi_w \equiv \angle \hat{w}$ , respectively. These phase shifts are found from the argument of the discrete Fourier transform of the velocity signals from (4.4). Samples of the phase shifts are taken at a height of 12 units above the turbulence virtual origin,  $z^+ + \ell_T^+ \approx 12$ , from the DNSs of smooth walls (figure 14a,f) and blade (▬▬▬) riblets (figure 14b–e,g–j). For the wavelengths considered ( $10 \leq \lambda_y^+ \leq 60$ ), the uniform p.d.f.s (white regions) for the smooth and  $\ell_g^+ \approx 5$  blade riblets (figure 14a,b,f,g) demonstrate that the flow signals shift between  $-\pi$  and  $\pi$  at equal probability, indicative of unconstrained turbulent motions for these scales. This further demonstrates that the turbulent flow is smooth-wall like above riblets of this size. For  $8 \lesssim \ell_g^+ \lesssim 16$  (figure 14c,d,h,i), we observe that wavelengths close to the riblet spacing,  $\lambda_y^+ \approx s^+$  (—) are pinned by the riblet textures, indicated by the varying p.d.f. along  $-\pi$  to  $\pi$ . As these pinned wavelengths increase with riblet spacing towards the average diameters of quasi-streamwise vortices ( $d^+ \approx 25$ , Kim *et al.* 1987; Robinson 1991; Jeong *et al.* 1997), the textures begin to interfere with these vortex scales, disrupting the smooth-wall-like behaviour of the cross-flow velocity fields. A small interference at this scale is seen for the  $w$  phase shifts  $\phi_w$  of  $\ell_g^+ \approx 10$  riblets ( $\lambda_y^+ \approx 2s^+ \approx 30$ , figure 14i), indicating that pinning may be a mechanism resulting in the onset of departure from smooth-wall-like flows at  $\ell_g^+ \approx 10$  (figure 6). For the riblets of size  $\ell_g^+ \approx 16$  (figure 14e,f), the peaks observed in the p.d.f.s of  $\phi_v$  and  $\phi_w$  for  $\lambda_y^+ \approx 25$  indicate that the scales of quasi-streamwise vortices are now pinned by the textures (Choi *et al.* 1993; Lee & Lee 2001). The pinning of vortices was thought to stabilise the streamwise streaks (Goldstein *et al.* 1995; Goldstein & Tuan 1998), which thereby explained how smaller riblets reduced drag. However, figure 14(e,j) shows

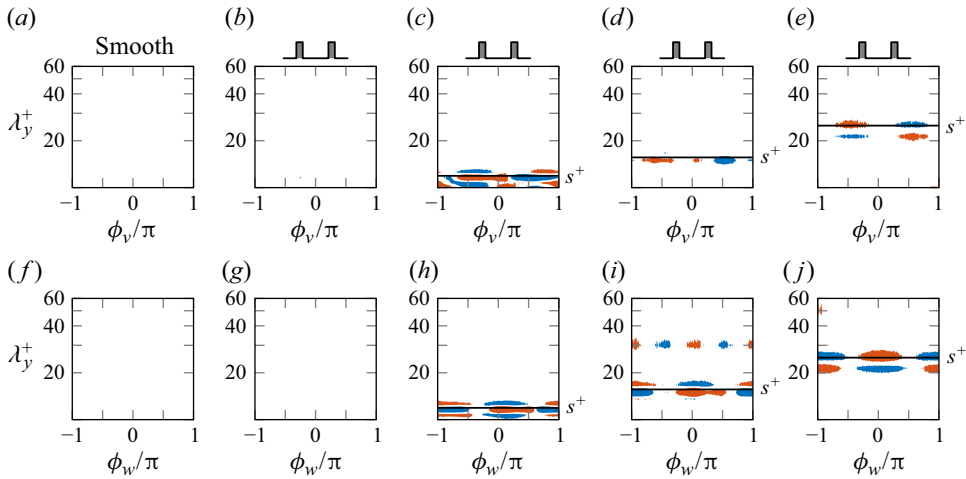


Figure 14. Probability density functions of the phase shifts of  $v$  and  $w$  fluctuations ( $\phi_v$  and  $\phi_w$ , respectively) as a function of wavelength,  $\lambda_y^+$ , at  $z^+ + \ell_T^+ \approx 12$ . These shifts quantify the spanwise location of the flow structures of various sizes  $\lambda_y^+$  in the  $yz$ -plane. The cases considered are (a,f) full-span smooth wall (SF395), and blade (▭) riblets of sizes (b,g)  $\ell_g^+ \approx 5$ , (c,h)  $\ell_g^+ \approx 8$ , (d,i)  $\ell_g^+ \approx 10$  and (e,j)  $\ell_g^+ \approx 16$ . For each  $\lambda_y^+$ , white regions indicate a p.d.f. of 0.5 where phase shifts are of equal probability, indicating the turbulent scales are unpinned by the wall. Regions bounded by red contours are where the p.d.f. is above 0.6, and blue contours are where the p.d.f. is less than 0.4, which shows that the turbulent scales are pinned by the riblet textures, particularly when the wavelength is approximately the size of the riblet spacing,  $\lambda_y^+ \approx s^+$ , indicated by a solid black line (—).

that vortex pinning is only active for the larger (post-optimal) riblets ( $\ell_g^+ \gtrsim 10$ ), suggesting that pinning is actually associated with drag increase (see also § 5.1 of García-Mayoral & Jiménez 2011b).

From the analysis above, the quasi-streamwise vortices ( $d^+ \approx 25$ ) are unpinned above riblets with sizes below the optimal,  $\ell_g^+ \lesssim 10.7$ . We incorporate this unpinned character of vortices in the viscous vortex model by uniformly averaging the solutions at all spanwise locations of the riblets relative to the vortex. We quantify the relative spanwise position by  $\Delta$  through a related spanwise coordinate  $\eta = y + \Delta$ , which has an origin at a riblet crest (figure 11). Here, the coordinate  $y$  is fixed to the location of zero wall-normal velocity at the upper boundary, i.e.  $w(y = 0, h) = 0$  (blue line, figure 11), and  $\Delta$  is the horizontal shift of the wall relative to  $y$ . Hence, increasing  $\Delta$  horizontally shifts the wall whilst fixing the top velocity boundary condition. Figures 15(a)–15(c) show the solution fields for the spanwise and wall-normal velocities and the streamwise vorticity for  $\Delta = 0$  (no shift, filled contours) and  $\Delta = s/2$  (half-riblet-spacing shift, solid line contours) for the two-scale trapezoidal riblets with  $\ell_g^+ \approx 5.5$ , or  $s^+ = 10$ , where  $s^+$  is computed using (4.3). Near the top, the solutions are similar for the various shifts of  $\Delta$  because of the same prescribed top boundary conditions. However, differences are seen near the wall, particularly for the vorticity (figure 15c), where we observe local peaks in vorticity near the crests. These peaks are also observed in the instantaneous flow fields of Lee & Lee (2001), which were previously characterised as the centres of vortices. However, the Stokes solution in figure 15(c) suggests that these peaks are instead caused by a rapid change in velocity due to the no-slip crests.

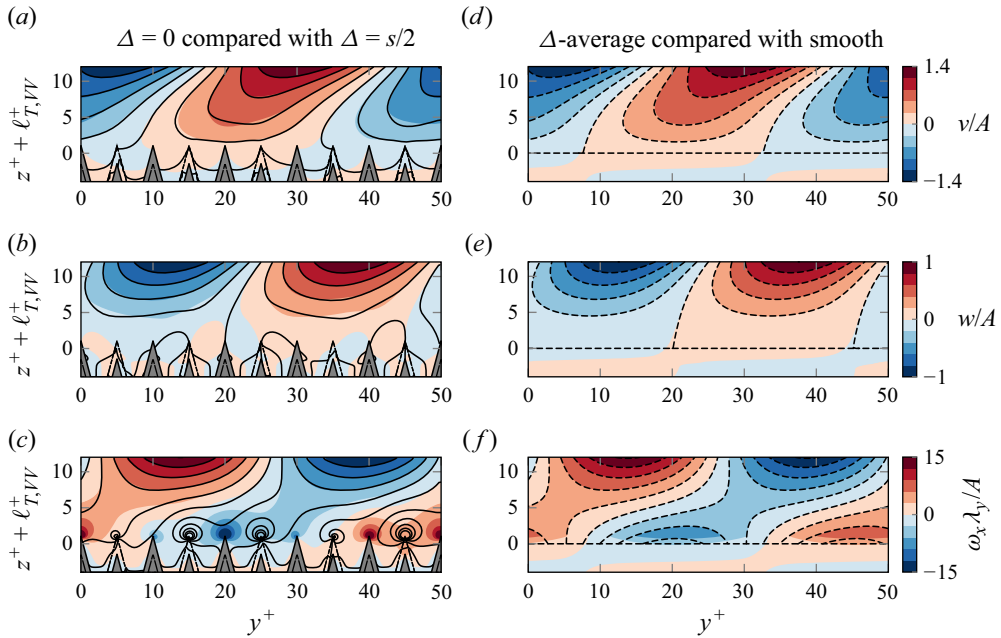


Figure 15. The Stokes solution fields of (top to bottom) spanwise velocity ( $v$ ), wall-normal velocity ( $w$ ) and streamwise vorticity ( $\omega_x = \partial w/\partial y - \partial v/\partial z$ ) for the two-scale trapezoidal (▬) riblets with  $\ell_g^+ \approx 5.5$  ( $s^+ = 10$ ), where  $s^+$  is computed using (4.3). (a–c) Two-scale riblet solutions for  $\Delta = 0$  (filled contours, grey riblets) are compared with that for  $\Delta = s/2$  (—, phantom-lined riblets); (d–f) average two-scale riblet solutions for all  $0 \leq \Delta < s$  (filled contours) show a collapse with the smooth wall (---) above the riblet crest plane, after a vertical offset by  $\ell_{T,VV}^+$ .



Using these two linearly independent solutions ( $\Delta = 0$  and  $\Delta = s/2$ ), we can analytically obtain additional solutions for any other  $\Delta$  (see Appendix C for more details). We then uniformly average the solutions in the range  $0 \leq \Delta < s$ , i.e. one riblet period by

$$\{v, w, \omega_x\}(y, z) = \frac{1}{s} \int_0^s \{v_\Delta, w_\Delta, \omega_{x,\Delta}\}(\Delta, y, z) d\Delta, \quad (4.8)$$

where  $(\cdot)_\Delta$  denotes the Stokes solution for a given  $\Delta$ . The phase-averaged solutions for the same two-scale trapezoidal riblets with  $\ell_g^+ \approx 5.5$  are illustrated in figures 15(d)–15(f) where each are compared with the equivalent smooth-wall case. Here, the value of  $\ell_{T,VV}^+$  is determined by negatively offsetting the riblet domain height by a guessed value of  $\ell_{T,VV}^+$ , and then iterating on this value until the r.m.s. streamwise vorticity,  $\omega'_x$ , matches with that above the equivalent smooth wall at the local minimum (i.e.  $z^+ + \ell_{T,VV}^+ \approx 5$ ). After matching  $\omega'_x$  at the local minimum, we also observe that the phase-averaged  $v$ ,  $w$  and  $\omega_x$  collapse everywhere above the riblet crest plane ( $z^+ > 0$ , figure 15d–f), which reflects the collapse of the DNS r.m.s. profiles in figure 9(b,d). The collapse also reaffirms the smooth-wall-like flow above riblets, even in regions close to the wall, after accounting for the unpinned character of quasi-streamwise vortices.

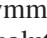


4.4. Drag predictions for riblets

In [figure 16](#), we report the turbulence virtual origin calculated by the viscous vortex model,  $\ell_{T,VV}^+$ , for all riblet geometries from [table 2](#), and for blade riblets () by [García-Mayoral & Jiménez \(2011a,b\)](#). [Figure 16\(a\)](#) shows the comparison between the modelled  $\ell_{T,VV}^+$  and the DNS  $\ell_T^+$  using a ratio between the two,  $\ell_T^+/\ell_{T,VV}^+$ . Here, we observe that  $\ell_{T,VV}^+$  differs from  $\ell_T^+$  in the range of 1%–10% for all present riblet geometries below the optimal size. This difference is noticeably less than  $\ell_T^+/h_\perp^+$  where the error in predicting  $\ell_T^+$  becomes larger (up to 40% at the optimal) with increasing size, because  $h_\perp^+$  is applicable only for vanishingly small riblets ([figure 7b](#)). For larger (post-optimal) riblets, the increased error in  $\ell_{T,VV}^+$  can be attributed to the departure from a smooth-wall-like turbulence as well as the pinning of quasi-streamwise vortices, both of which are not accounted for in the viscous vortex model. [Figures 16\(b\)–16\(i\)](#) show the magnitudes of  $\ell_T/\ell_g$  from DNS (coloured filled symbols),  $\ell_{T,VV}/\ell_g$  from the viscous vortex model (open white symbols and black fitted lines), and  $h_\perp/\ell_g$  from the protrusion-height model (grey lines) as a function of  $\ell_g^+$ . For each riblet shape, we compute  $\ell_{T,VV}/\ell_g$  for several riblet sizes, then use a best-fit line to obtain  $\ell_{T,VV}/\ell_g$  for a continuous range of riblet sizes. We observe that the viscous vortex model also predicts  $\ell_T^+ \rightarrow h_\perp^+$  for vanishingly small riblets ( $\ell_g \rightarrow 0$ ) (, [figure 16b](#)), tending towards the same output as the protrusion-height model ([Luchini et al. 1991](#); [Luchini 1996](#)). Hence,  $\ell_{T,VV}^+$  for any riblet size  $\ell_g^+$  can be approximated as

$$\ell_{T,VV}^+ = h_\perp^+ + m_T \ell_g^{+2}, \tag{4.9}$$

where  $m_T$  is the gradient of the (empirical) best-fit line of  $\ell_{T,VV}/\ell_g$  against  $\ell_g^+$  for a given riblet shape. This gradient,  $m_T$ , can be computed by using at least two data points for a given riblet shape (e.g. [figure 16d](#)): (i)  $h_\perp/\ell_g$  from the protrusion-height model for  $\ell_g^+ = 0$ , and (ii)  $\ell_{T,VV}/\ell_g$  for one riblet size below the optimum. In [figure 16](#), we observe that  $m_T$  decreases with increasing height-to-spacing ratio, especially obvious for the triangular riblets with systematically varied tip angle  $\alpha = 30^\circ, 60^\circ, 90^\circ$  ([figure 16d–f](#)). Here, a larger  $m_T$  is associated with a larger  $\Delta U^+$  deviation from the linear protrusion-height model ([3.1](#)) at matched  $\ell_g^+$ , as observed in [figure 3\(a\)](#).

[Figure 16\(g\)](#) shows two calculations of  $\ell_{T,VV}/\ell_g$  at matched sizes for the asymmetric triangle riblets (). Due to the asymmetric nature of the riblets, the Stokes solutions may differ depending on the direction of rotation of the modelled vortex. Here, we computed the additional  $\ell_{T,VV}/\ell_g$  by reversing the direction of the modelled vortex, i.e. changing the signs of [\(4.2\)](#). These two  $\ell_{T,VV}/\ell_g$  differ only by 2%, and hence, the direction of rotation of the modelled vortex does not significantly affect  $\ell_{T,VV}/\ell_g$  for the asymmetric riblets.

Equation [\(4.9\)](#) is a second-order polynomial fit to the viscous vortex model, distinct from second- or higher-order asymptotic expansions in homogenisation. Higher-order asymptotic expansions formally require a scale ratio of riblets to turbulence approaching zero for convergence. Even the smallest coherent turbulent scales ( $\approx 30$ , such as the diameter of a near-wall vortex core) are of the order of the optimal riblet size,  $s^+ \approx 15$ . At such a finite ratio, adding more terms need not improve the approximation of the expansion ([Bender & Orszag 1978](#)). As such, higher-order homogenisation techniques are formally invalid for finite viscous-scaled riblet textures ([Ibrahim et al. 2021](#)). The present analysis also suggests that formal expansions, if successfully attempted, would inevitably involve tackling the nonlinear interactions of the flow that sets the model parameters ( $A, B, \Phi$  and  $\lambda_y^+$ ), noting that even the well-known streak spacing has not been calculated by any

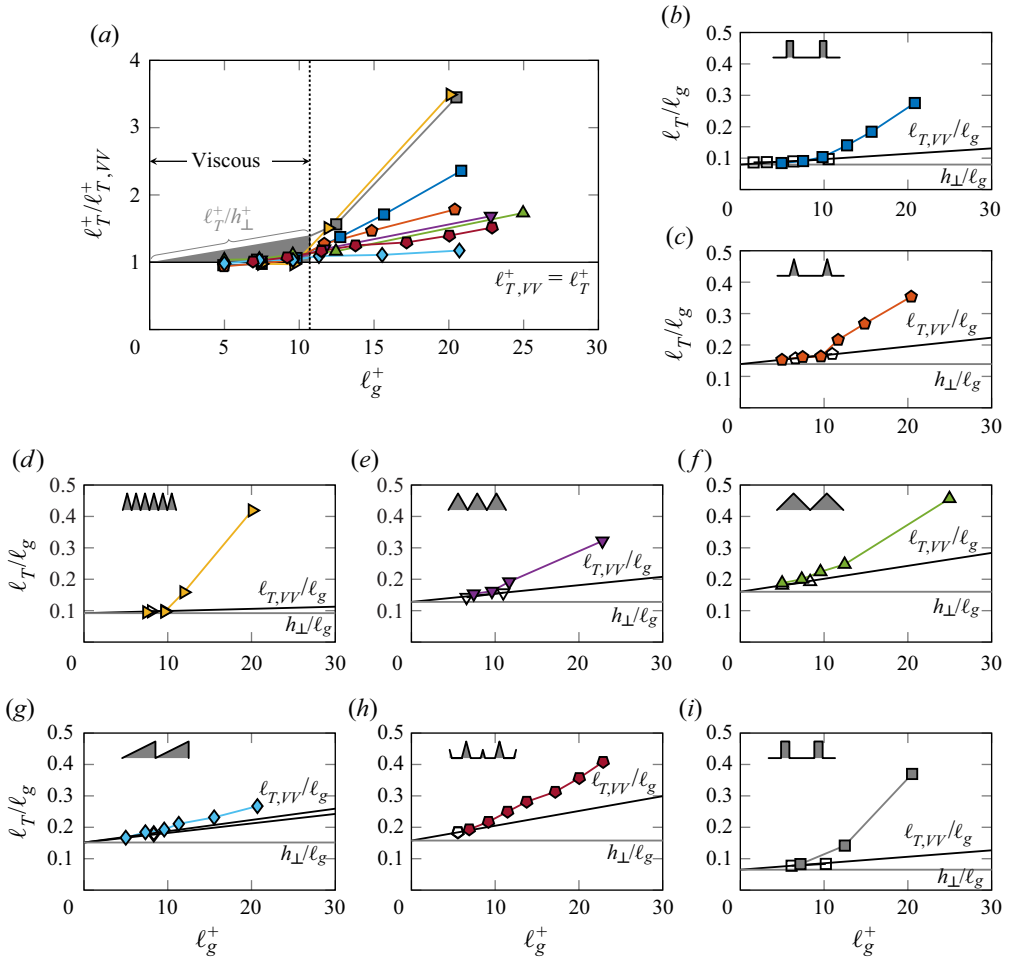


Figure 16. (a) Ratios of the observed  $\ell_T^+$  from DNS to the calculated  $\ell_{T,VV}^+$  show that the present model accurately predicts  $\ell_T^+$  for sizes below the optimum,  $\ell_g^+ \lesssim 10.7$ . For convenience, the grey region indicates the range of  $\ell_T^+/h_\perp^+$ , as in figure 7(b). (b–i) Turbulence virtual origin per unit  $\ell_g$ ,  $\ell_T/\ell_g$ , as a function of riblet size,  $\ell_g^+$ . Coloured markers represent data from DNS, open markers are outputs of the viscous vortex model,  $\ell_{T,VV}/\ell_g$ , with a corresponding linear best-fit line (solid black). Solid grey lines indicate the spanwise protrusion height,  $h_\perp/\ell_g$ .

formal mathematical procedure. In other words, unless introduced explicitly, obtaining these model parameters requires modelling the self-sustaining process. Instead, here, we use the mean information from the nonlinear flow to retain the use of linear viscous equations in the spirit of Luchini *et al.* (1991). The present approach effectively bypasses the aforementioned challenges by recognising that the nonlinearity is similar regardless of the wall conditions (i.e. smooth-wall like), and thereby, requires us to determine the flow properties only once. Correspondingly, the ability of the present approach to accurately predict  $\ell_T^+$  indicates that the essential physics have been captured.

With the accurate prediction of  $\ell_T^+$  at non-vanishing riblet sizes, we can now predict the drag reduction,  $\Delta U^+$ . As  $-\Delta U^+ \approx \ell_V^+ - \ell_T^+$  (figure 5d) and  $\ell_V^+ \approx h_\parallel^+$  (figure 7a), the

drag prediction of the model can be written as

$$-\Delta U_{VV}^+ = h_{\parallel}^+ - \ell_{T,VV}^+, \quad (4.10)$$

by simply replacing  $h_{\perp}^+$  with  $\ell_{T,VV}^+$  in (3.1). Similar to the protrusion-height model, (4.10) consists of *a priori* quantities, which are solely based on a given riblet shape and size below the optimal ( $\ell_g^+ \lesssim 10.7$ ). In figure 17, we note that  $\Delta U_{VV}^+$  for all riblet shapes agree with  $\Delta U^+$  measured from the present DNS, and from DNSs and wall-resolved LES of past studies (El-Samni *et al.* 2007; García-Mayoral & Jiménez 2011*b*, 2012; Bannier *et al.* 2015; Li & Liu 2019; Malathi *et al.* 2022; Cipelli 2023), for riblet sizes up to  $\ell_g^+ \approx 10.7$ . However, the experimental drag reduction of triangular and trapezoidal riblets from Bechert *et al.* (1997), shown in figure 17(*b,e,f,i*), generally exhibits lower magnitudes compared with DNS/wall-resolved LES data. Experimental drag-reduction measurements have been converted to  $\Delta U^+$  based on matched bulk Reynolds number following from Bechert *et al.* (1997),  $\Delta C_f/C_{f0} \approx \Delta U^+ / [(2C_{f0})^{-1/2} + (2\kappa)^{-1}]$  using  $\kappa = 0.4$ . Some error will be introduced into the converted  $\Delta U^+$  values as the experiments were conducted in an asymmetric channel set-up (one smooth and one riblet wall). Nonetheless, considering figure 17(*b*), there is a 30% discrepancy in the optimal performance of trapezoidal riblets (▲▲) between the experimental and DNS data. A source of this discrepancy is the finite width of the milled riblet tips (e.g. ▲▲), with tip bluntness having been shown to decrease drag performance (Walsh 1990; Bechert *et al.* 1997; García-Mayoral & Jiménez 2011*a*; Grüneberger & Hage 2011). While Bechert *et al.* (1997) did not provide measurements of the width of the trapezoidal (and triangular) riblet tips, the manufacturing tolerance can be estimated based on tip measurements of scalloped riblets (figure 9 of Bechert *et al.* 1997), as  $R/s \approx 0.01$ – $0.02$  or  $R \approx 0.03$ – $0.11$  mm, where  $R/s$  represents the ratio of effective tip radius  $R$  to the riblet spacing  $s$ . Assuming a similar manufacturing tolerance for trapezoidal riblets implies  $R/s \approx 0.03$  (▲▲), or  $R = 0.13$  mm based on the provided  $s = 4$  mm spacing (figure 24 of Bechert *et al.* 1997). With  $R/s \approx 0.03$ , the viscous vortex model would predict a degradation in optimal performance of  $\approx 15\%$  (figure 17*b*), accounting for half of the observed 30% discrepancy. Grüneberger & Hage (2011) repeated measurements using sharper flat-tipped trapezoidal riblets (equivalent to  $R/s \approx 0.003$ – $0.005$ ) with  $\alpha = 45^\circ$  in the same testing facility, and obtained better agreement with both the protrusion-height model and  $\Delta U_{VV}^+$  (figure 17*i*), given the smaller  $R/s$ . A similar level of accuracy is observed when comparing the experimental data of von Deyn *et al.* (2022), depicted in figure 17(*j*), whose riblets were manufactured to a tolerance of  $R/s \approx 0.002$ . Another source of disagreement with Bechert *et al.* (1997) is an unmatched bulk Reynolds number. Small changes in the effective channel height have been shown to significantly change  $-\Delta U^+$  (von Deyn *et al.* 2022). Adjusting the experimental drag curve of Bechert *et al.* (1997) for the trapezoidal riblets (▲▲) using an effective channel height starting from  $z^+ = -\ell_{T,VV}^+$  compared with that from  $z^+ = -0.4k^+$  (figure 24 of Bechert *et al.* 1997) results in a 5% increase in  $-\Delta U_{opt}^+$ . Other sources of discrepancy include the finite fetch of the riblet test plate (cf. Garratt 1990; García-Mayoral & Jiménez 2011*a*), and the unflushed transition from smooth channel to riblet test plates which induces pressure drag (cf. Bechert, Bruse & Hage 2000; Spalart & McLean 2011; Li *et al.* 2019; Smith, Yagle & McClure 2023).

As (4.10) is quadratic in  $\ell_g^+$ , the departure near the optimum from linearity of the extrapolated protrusion-height model (by up to 40%, figure 3*a*) can also be captured. Figure 18 compares (4.10) and the extrapolated protrusion-height model (3.1) against the optimal drag reduction  $\Delta U_{opt}^+$  obtained from the DNS/wall-resolved LES. Here, the

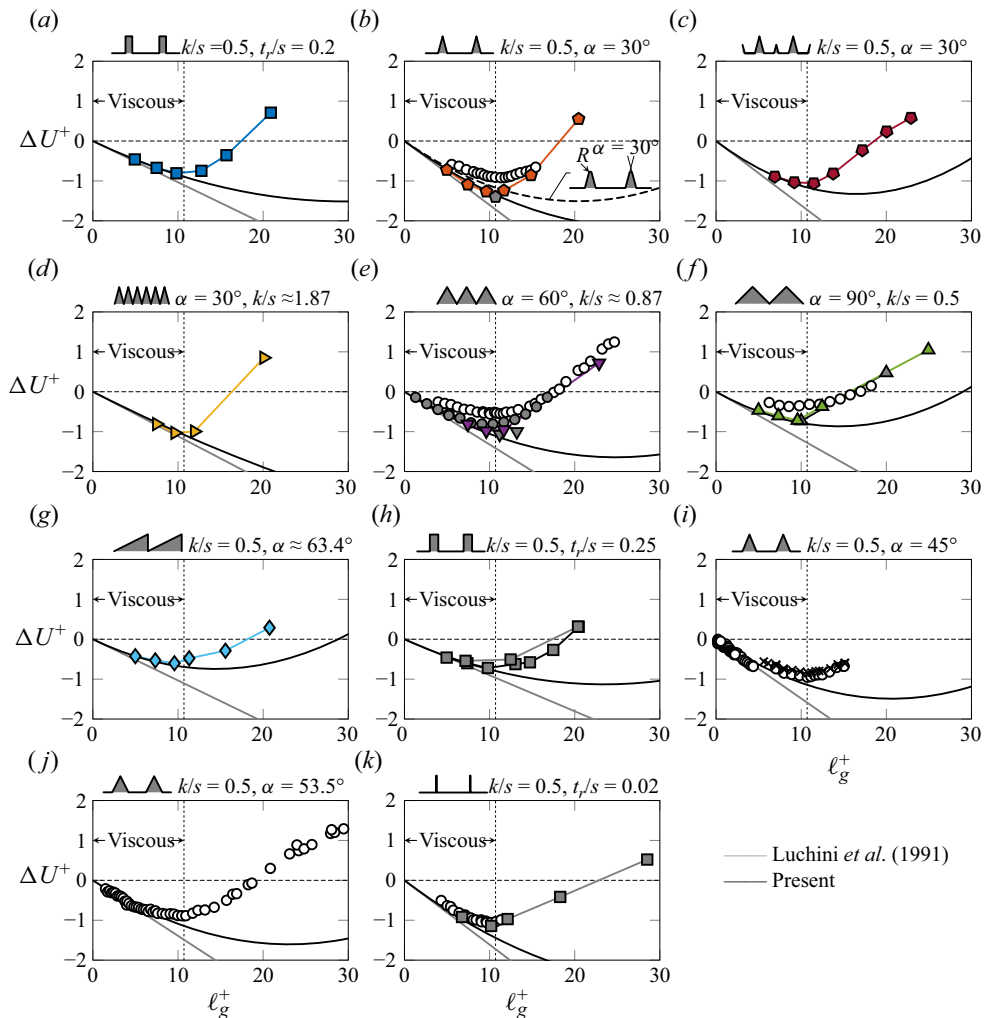


Figure 17. Roughness function  $\Delta U^+$  of riblets as a function of riblet groove size,  $\ell_g^+$ . Roughness functions measured from DNS (coloured symbols) are compared with the linear protrusion-height model of Luchini *et al.* (1991) (—, grey) and the present drag prediction (4.10) for perfectly sharp riblets (—) and a tip-rounded trapezoidal riblet with  $R/s \approx 0.03$  and  $k/s \approx 0.4$  (---) in (b). Grey markers are LES/DNS results from (b) Bannier *et al.* (2015), (e) Choi *et al.* (1993), Malathi *et al.* (2022), Cipelli (2023), (f) Li & Liu (2019), (h) García-Mayoral & Jiménez (2011*b*, 2012) and (k) El-Samni *et al.* (2007). White circles (o) are experimental  $\Delta U^+$  from (b,e,f,k) Bechert *et al.* (1997), (i) Grüneberger & Hage (2011) and (j) von Deyn *et al.* (2022). Crosses (x) in (i) are from Bechert *et al.* (1997). These experimental  $\Delta U^+$  data, except for von Deyn *et al.* (2022), are obtained by adjusting the percentage drag reduction  $DR$  based on the respective flow conditions.

riblet sizes are determined by the optimal drag reduction from the DNS and LES data. In figure 18(a), the overprediction of optimal drag reduction up to 40% in the extrapolated protrusion-height model is somewhat mitigated by applying an empirical factor of 0.83 (García-Mayoral & Jiménez 2011*a,b*), which instead leaves a discrepancy of  $\pm 20\%$  among different riblet geometries. Note that, in the original work of Luchini *et al.* (1991), it was never suggested that the protrusion-height model could be used to predict  $\Delta U_{opt}^+$ , but was only intended to be valid for vanishingly small riblets. In figure 18(b), we observe that

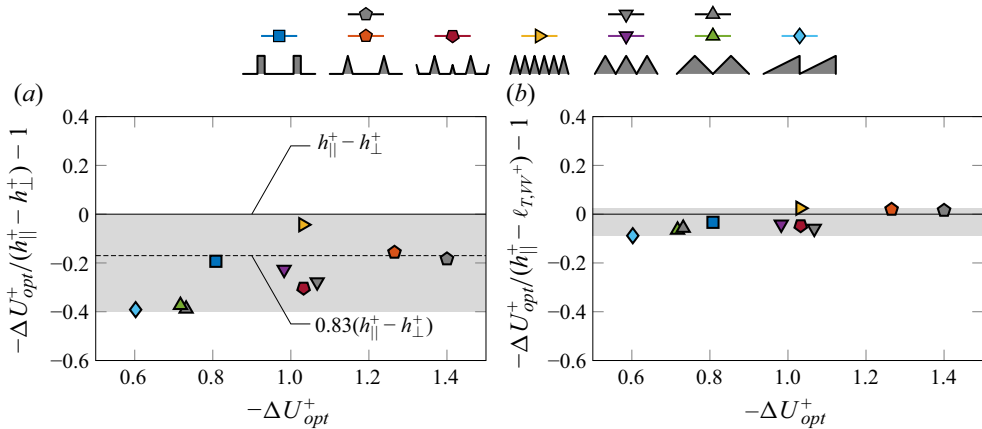


Figure 18. Optimal riblet drag reduction obtained from DNS,  $\Delta U_{opt}^+$ , compared with (a) an extrapolation of the protrusion-height model to the optimal size, and (b) the present drag-reduction prediction in (4.10). Markers indicate different riblet shapes consistent with figure 17. Riblet sizes are  $10 \lesssim \ell_g^+ \lesssim 11$  depending on the optimal drag reduction available in the dataset.

replacing  $h_{\perp}^+$  with  $\ell_{T,VV}^+$  further improves the optimal drag prediction, and alleviates the 40% overprediction from before.

## 5. Conclusion

In this paper, we present a flow-structure-based model governed by the steady, two-dimensional Stokes equations to accurately predict the drag performance,  $\Delta U^+$ , of small riblets up to the optimal groove size  $\ell_g^+ \lesssim 10.7$  (figure 18). We first note that the flow above these riblets remains essentially smooth-wall like (figures 5b,d and 6), such that the drag performance is the difference in offsets of the mean flow and turbulence,  $-\Delta U^+ = \ell_U^+ - \ell_T^+$  (Garcia-Mayoral *et al.* 2019; Ibrahim *et al.* 2021). As the mean-flow offset can be accurately captured by the longitudinal protrusion height of Luchini *et al.* (1991),  $h_{||}^+ = \ell_U^+$  (figure 7a), the present model solely predicts the turbulence offset,  $\ell_T^+$ , which the spanwise protrusion height is unable to accurately predict near the optimal riblet size, that is  $h_{\perp}^+ < \ell_T^+$ , as shown in figure 7(b).

As transpiration effects are negligible for vanishingly small riblets, the protrusion-height model can accurately predict the limiting gradient of the drag reduction. However, transpiration is relevant once the quasi-streamwise vortex can induce flow that penetrates the grooves of larger riblets. We show that transpiration is crucial at non-vanishing riblet sizes by evaluating an empirical fit for  $\ell_T^+$  (3.3) that includes transpiration effects (Ibrahim *et al.* 2021) and that agrees with  $\ell_T^+$  from the present DNSs of riblets (figure 8b). However, the empirical fit (3.3) requires *a posteriori* measurements from the riblet DNS r.m.s. velocities. To predict  $\ell_T^+$  without DNS, here we take another approach in the spirit of the protrusion-height model by introducing a wall-normal velocity component due to a quasi-streamwise vortex.

The present model, which we term the viscous vortex model, represents an averaged near-wall response from the overlying quasi-streamwise vortex (representing turbulence) in the cross-plane. It allows for a given turbulent scale to interact with a non-vanishing riblet size, as opposed to previous homogenisation strategies that require vanishingly small textures. Furthermore, an explicit model of the self-sustenance of the quasi-streamwise

vortex is not needed, since we only model the region dominated by viscosity near the wall. As such, the viscous vortex model is governed by the Stokes equations (4.1) with the appropriate domain size and boundary conditions (figure 11). By exposing the riblets to a vortical flow structure, modelled by spanwise-varying sinusoidal waves for the spanwise and wall-normal velocities (4.2) at the top of the domain, the crucial crest-transpiration effect is readily induced (figure 15*b*). The amplitudes and the phase shift of (4.2) are determined from a Fourier analysis of the cross-flow velocities in the DNS. As riblets exhibit smooth-wall-like flows, these amplitudes and phase shift are the same as that of the smooth wall at matched height relative to the turbulence virtual origin (figure 13*d–f*), demonstrating that DNSs of riblets are not required to formulate (4.2). Additionally, we uniformly average the solutions across spanwise shifts of the riblet wall to account for the unpinned character of quasi-streamwise vortices above riblet grooves, which is corroborated by uniform p.d.f.s of DNS cross-flow velocity phase shifts for riblets below the optimal size (figure 14). By incorporating these effects, the viscous vortex model is able to accurately predict  $\ell_T^+$  for riblets up to the optimal size (figure 16). We further propose an expression for  $\ell_T^+$  for a given riblet shape in (4.9) to determine the drag prediction as a function of size,  $\ell_g^+$ , in (4.10). The present model accurately predicts the drag performance of riblets up to the optimal size,  $\ell_g^+ \lesssim 10.7$  (figure 18*b*) and alleviates the aforementioned 40% discrepancy for optimal drag prediction that arises from assuming that  $\ell_T^+ = h_{\perp}^+$ .

Beyond the optimal size ( $\ell_g^+ \gtrsim 10.7$ ), the present drag prediction,  $\Delta U_{VV}^+$ , does not capture the breakdown of the drag curve (figure 17). In this post-optimal region ( $\ell_g^+ \gtrsim 10.7$ ), García-Mayoral & Jiménez (2011*b*) observed a rapid increase in the near-wall Reynolds stress, which departs from smooth-wall-like turbulence and contributes to the further increase in drag. The viscous vortex model, which only accounts for smooth-wall-like turbulence, does not capture this increase in Reynolds stress. Here, non-smooth-wall-like modifications such as Kelvin–Helmholtz rollers (García-Mayoral & Jiménez 2011*b*) have been proposed, but other mechanisms are also active (Endrikat *et al.* 2021*a*; Modesti *et al.* 2021). Resolvent-based models for riblets (Chavarin & Luhar 2020; Ran, Zare & Jovanović 2021) have also been shown to capture these non-smooth-wall-like mechanisms, which may provide avenues to model the full drag performance curve of riblets.

**Acknowledgements.** The authors gratefully acknowledge the anonymous reviewers for their comments on the manuscript.

**Funding.** The authors gratefully acknowledge the support of the Air Force Office of Scientific Research under award number FA2386-21-1-4018 (program managers: D.J. Newell and R.W. Carr, AOARD). We also thank D.R. Smith (EOARD) and G.L. Abate (AFOSR). This work is supported by the Australian Research Council Discovery Project DP170102595, and with the assistance of resources from NCI that is supported by the Australian Government and from Pawsey that is funded by the Australian Government and the Government of Western Australia.

**Declaration of interests.** The authors report no conflict of interest.

**Author ORCIDs.**

- ✉ J. Wong <https://orcid.org/0000-0002-1752-4076>;
- ✉ C.J. Camobreco <https://orcid.org/0000-0001-7068-3204>;
- ✉ R. García-Mayoral <https://orcid.org/0000-0001-5572-2607>;
- ✉ N. Hutchins <https://orcid.org/0000-0003-1599-002X>;
- ✉ D. Chung <https://orcid.org/0000-0003-3732-364X>.



### Appendix A. Measurement of Clauser–Hama roughness function at mismatched Reynolds number

The roughness function  $\Delta U^+$  is the vertical shift in the velocity profile between riblet and smooth walls in the log and wake regions at matched  $Re_\tau$ . Since we do not have an infinitely large  $Re_\tau$  for our DNS, the Reynolds number effect on the log region may be significant if  $Re_\tau$  is not exactly matched with the smooth wall (figure 19), which leads to an inaccurate measurement of  $\Delta U^+$  (Gómez-de-Segura *et al.* 2018a). We demonstrate the analytical calculation of  $\Delta U^+$  by first deriving the velocity profiles of riblet and smooth wall using the mean turbulent momentum balance equation for fully developed channel flow

$$0 = -\frac{1}{\rho} \frac{dP}{dx} + \nu \frac{d^2 U}{dz_*^2} - \frac{\overline{u'w'}}{dz_*}, \quad (A1)$$

where  $(z_*)$  refers to the respective wall-normal coordinate for smooth wall ( $z$ ) or riblet wall ( $z_T$ ),  $(\cdot)$  denotes plane and time mean and  $U$  is the plane and time mean streamwise velocity. The relationship between the imposed pressure gradient,  $dP/dx$  and the drag per plan area,  $\tau_w$  can be found through a force balance of the control volume containing the channel fluid

$$-\frac{1}{\rho} \frac{dP}{dx} = \frac{1}{\rho} \frac{\tau_w}{\delta} > 0, \quad (A2)$$

where  $\delta$  is the half-channel height measured from smooth wall,  $\delta_s$  or mean riblet height,  $\delta_r$  (see figure 19). For a smooth wall, (A1) is valid from  $z = 0$  to  $\delta_s$ , whilst for a riblet wall, the equation is valid from  $z_T = \ell_T$  to  $\delta'_r$ , supposing that the origin of turbulence,  $\ell_T$ , is known for the moment. Combining (A1) and (A2), and separating the analysis to smooth ( $s$  subscript) and riblet ( $r$  subscript)

$$\frac{d}{dz} \left( \nu_s \frac{dU_S}{dz} - \overline{u'w'_S} \right) = -\frac{\tau_{ws}}{\rho_s} \frac{1}{\delta_s} \quad \frac{d}{dz_T} \left( \nu_r \frac{dU_R}{dz_T} - \overline{u'w'_R} \right) = -\frac{\tau_{wr}}{\rho_r} \frac{1}{\delta_r}, \quad (A3a,b)$$

where the drag per plan area  $\tau_{ws}$ , fluid density  $\rho_s$ , half-channel height  $\delta_s$  and kinematic viscosity  $\nu_s$  are for the smooth-wall simulation;  $\tau_{wr}$ ,  $\rho_r$ ,  $\delta_r$  and  $\nu_r$  are for the riblet-wall simulation. These simulations are independent of each other, hence we perform the mathematical analysis separately. First, we can obtain the total stress profile by integrating (A3) once with respect to  $z$  or  $z_T$ . Using the imposed free-slip boundary condition at the top domain (figure 19), we

$$\left. \begin{array}{l} \text{integrate both sides of (A3a)} \\ \text{from } z = z \text{ to } \delta_s: \\ \text{B.C.: } \left( \nu_s \frac{dU_S}{dz} - \overline{u'w'_S} \right) \Big|_{z=\delta_s} = 0 \\ \Rightarrow \nu_s \frac{dU_S}{dz} - \overline{u'w'_S} = \frac{\tau_{ws}}{\rho_s} \left( 1 - \frac{z}{\delta_s} \right) \end{array} \right\} \quad \left. \begin{array}{l} \text{integrate both sides of (A3b)} \\ \text{from } z_T = z_T \text{ to } \delta'_r: \\ \text{B.C.: } \left( \nu_r \frac{dU_R}{dz_T} - \overline{u'w'_R} \right) \Big|_{z_T=\delta'_r} = 0 \\ \Rightarrow \nu_r \frac{dU_R}{dz_T} - \overline{u'w'_R} = \frac{\tau_{wr}}{\rho_r} \frac{\delta'_r - z_T}{\delta_r}. \end{array} \right\} \quad (A4a,b)$$

In order to obtain profiles at similar scales, we normalise (A4) using the imposed kinematic viscosity,  $\nu_s$  or  $\nu_r$  and the effective friction velocity. The effective friction velocity squared,  $u_\tau^2$ , can be derived from the left-hand side of (A4a,b) where the total stress,  $\nu dU/dz_* - \overline{u'w'}$  is fully dominated by the viscous stress,  $\nu dU/dz_*$ , i.e. zero Reynolds stress. For the smooth wall, this location is non-arbitrary (i.e. at  $z = 0$ ) where we recover

$\nu_s dU_S/dz = \tau_{ws}/\rho_s$  from the right-hand side. For riblets, the location of the virtual wall perceived by the turbulence is at the origin of turbulence, where virtually, the Reynolds stresses vanishes (Gómez-de-Segura *et al.* 2018a; Fairhall *et al.* 2019; Ibrahim *et al.* 2021). Hence, the effective friction velocity of riblet walls is found by extrapolating the total stress line (A4b) to the origin of turbulence ( $z_T = 0$ ), i.e. evaluating the right-hand side of (A4b) at  $z_T = 0$  even though (A4b) is not defined there. The effective friction velocities for smooth and riblet walls are defined as

$$u_{\tau s} = \sqrt{\frac{\tau_{ws}}{\rho_s}} \quad u_{\tau r} = \sqrt{\frac{\tau_{wr}}{\rho_r} \frac{\delta'_r}{\delta_r}}, \tag{A5a,b}$$

where (A5b) is consistent with Ibrahim *et al.* (2021). Now we normalise (A4) into viscous units

$$\frac{d\left(\frac{U_S}{u_{\tau s}}\right)}{d\left(\frac{zu_{\tau s}}{\nu_s}\right)} - \frac{\overline{u'w'}_S}{u_{\tau s}^2} = 1 - \frac{\frac{zu_{\tau s}}{\nu_s}}{\frac{\delta_s u_{\tau s}}{\nu_s}} \quad \frac{d\left(\frac{U_R}{u_{\tau r}}\right)}{d\left(\frac{z_T u_{\tau r}}{\nu_r}\right)} - \frac{\overline{u'w'}_R}{u_{\tau r}^2} = 1 - \frac{\frac{z_T u_{\tau r}}{\nu_r}}{\frac{\delta'_r u_{\tau r}}{\nu_r}}, \tag{A6a,b}$$

where we observe the similarity in the total stress profiles when scaled with the appropriate friction velocity and kinematic viscosity. We integrate (A6) once more to obtain the velocity profiles. For a smooth wall, one may be inclined to integrate from the wall  $zu_{\tau s}/\nu_s = 0$  to an arbitrary wall-normal location,  $zu_{\tau s}/\nu_s$ . However, the lower limit for the riblet wall,  $z_T u_{\tau r}/\nu_r = \ell_T u_{\tau r}/\nu_r$ , is different, since the equation is only valid from the crest (refer to figure 19 to locate the crest relative to  $z$ ). We integrate (A6) using similar limits of integration, to simplify cancellations when taking the difference between the profiles. We first integrate the smooth profile starting from an arbitrary position,  $zu_{\tau s}/\nu_s = C$ ,

$$\left. \begin{array}{l} \text{integrate both sides of (A6a)} \\ \text{from } \frac{zu_{\tau s}}{\nu_s} = C \text{ to } \frac{zu_{\tau s}}{\nu_s}: \\ \text{B.C.: } \frac{U_S}{u_{\tau s}} \Big|_{zu_{\tau s}/\nu_s=C} = \frac{U_{SC}}{u_{\tau s}} \\ \Rightarrow \frac{U_S}{u_{\tau s}} = \frac{U_{SC}}{u_{\tau s}} - \frac{1}{2} \\ \times \left[ \frac{\left(\frac{zu_{\tau s}}{\nu_s}\right)^2}{\frac{\delta_s u_{\tau s}}{\nu_s}} - \frac{(C)^2}{\frac{\delta_s u_{\tau s}}{\nu_s}} \right] \\ + \frac{zu_{\tau s}}{\nu_s} - C \\ + \int_C^{zu_{\tau s}/\nu_s} \frac{\overline{u'w'}_S}{u_{\tau s}^2} d\left(\frac{zu_{\tau s}}{\nu_s}\right) \end{array} \right\} \begin{array}{l} \text{integrate both sides of (A6b)} \\ \text{from } \frac{z_T u_{\tau r}}{\nu_r} = \frac{\ell_T u_{\tau r}}{\nu_r} \text{ to } \frac{z_T u_{\tau r}}{\nu_r}: \\ \text{B.C.: } \frac{U_R}{u_{\tau r}} \Big|_{z_T u_{\tau r}/\nu_r = \frac{\ell_T u_{\tau r}}{\nu_r}} = \frac{U_{R0}}{u_{\tau r}} \\ \Rightarrow \frac{U_R}{u_{\tau r}} = \frac{U_{R0}}{u_{\tau r}} - \frac{1}{2} \\ \times \left[ \frac{\left(\frac{z_T u_{\tau r}}{\nu_r}\right)^2}{\frac{\delta'_r u_{\tau r}}{\nu_r}} - \frac{\left(\frac{\ell_T u_{\tau r}}{\nu_r}\right)^2}{\frac{\delta'_r u_{\tau r}}{\nu_r}} \right] \\ + \left(\frac{z_T u_{\tau r}}{\nu_r} - \frac{\ell_T u_{\tau r}}{\nu_r}\right) \\ + \int_{\ell_T u_{\tau r}/\nu_r}^{z_T u_{\tau r}/\nu_r} \frac{\overline{u'w'}_R}{u_{\tau r}^2} d\left(\frac{z_T u_{\tau r}}{\nu_r}\right). \end{array} \tag{A7a,b}$$

Equation (A7) is the analytical velocity profile given the boundary conditions of the top domain in figure 19 and the boundary condition at the lower limit, i.e. at  $zu_{\tau s}/\nu_s = C$  for smooth wall or  $z_T u_{\tau r}/\nu_r = \ell_T u_{\tau r}/\nu_r$  for riblet wall.

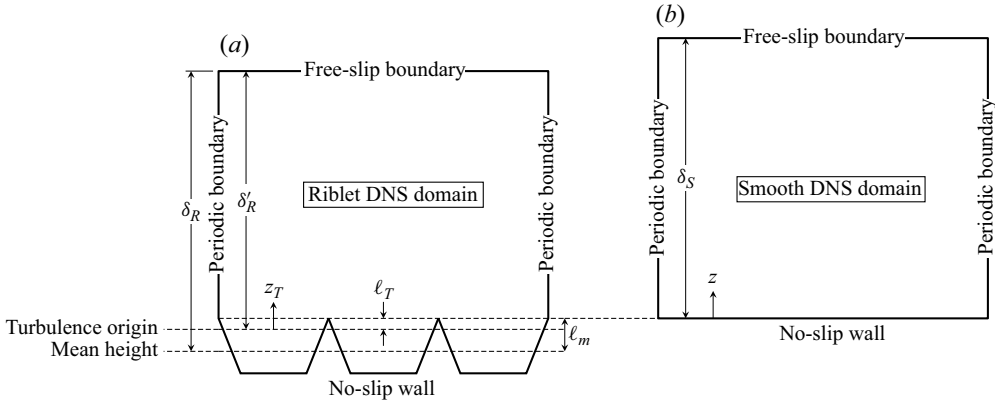


Figure 19. The streamwise uniform cross-plane for (a) riblets and (b) smooth wall with their boundary conditions and half-channel height measured from turbulence origin,  $\delta'_r$  (known after simulation) or mean height,  $\delta_r$  (prior-simulation input) and from smooth wall  $\delta_s$  (also set prior to simulation). The effective friction velocity,  $u_{\tau r}$ , measured from the origin of turbulence,  $z_T = 0$ , where  $\delta'_r$  is unknown prior to the simulation, causes a slight difference in the effective  $Re_{\tau}$  between riblet and smooth walls (i.e.  $\delta'_r u_{\tau r} / \nu_r \neq \delta_s u_{\tau s} / \nu_s$ ).

Now, we let  $C = \ell_T u_{\tau r} / \nu_r$  so that  $U_{SC} / u_{\tau s}$  can be found by evaluating (A7a) at  $z u_{\tau s} / \nu_s = 0$ , i.e. at the wall where  $U_S / u_{\tau s} = 0$

$$\frac{U_{SC}}{u_{\tau s}} = \frac{\ell_T u_{\tau r}}{\nu_r} - \frac{1}{2} \frac{\left( \frac{\ell_T u_{\tau r}}{\nu_r} \right)^2}{\delta_s u_{\tau s}} + \int_0^{\ell_T u_{\tau r} / \nu_r} \frac{\overline{u'w'_S}}{u_{\tau s}^2} d\left( \frac{z u_{\tau s}}{\nu_s} \right). \quad (\text{A8})$$

Therefore, the difference between smooth and riblet profiles at matched wall-normal height,  $z_{\Delta}^+ = z u_{\tau s} / \nu_s = z_T u_{\tau r} / \nu_r$ , is

$$\begin{aligned} \frac{U_S}{u_{\tau s}} - \frac{U_R}{u_{\tau r}} = & \underbrace{- \left( \frac{U_{R0}}{u_{\tau r}} - \frac{U_{SC}}{u_{\tau s}} \right)}_{\Delta U^+} - \frac{1}{2} \left[ z_{\Delta}^{+2} - \left( \frac{\ell_T u_{\tau r}}{\nu_r} \right)^2 \right] \underbrace{\left( \frac{1}{\delta_s u_{\tau s}} - \frac{1}{\delta'_r u_{\tau r}} \right)}_{\epsilon_{\Delta}^+} \\ & + \underbrace{\int_{\ell_T u_{\tau r} / \nu_r}^{z_{\Delta}^+} \frac{\overline{u'w'_S}}{u_{\tau s}^2} d\left( \frac{z u_{\tau s}}{\nu_s} \right) - \int_{\ell_T u_{\tau r} / \nu_r}^{z_{\Delta}^+} \frac{\overline{u'w'_R}}{u_{\tau r}^2} d\left( \frac{z_T u_{\tau r}}{\nu_r} \right)}_{\approx 0 \text{ for smooth-wall-like riblets}}. \end{aligned} \quad (\text{A9})$$

If we assume that the Reynolds stress profiles collapse when scaled to viscous units, i.e.  $\overline{u'w'_S} / u_{\tau s}^2 = \overline{u'w'_R} / u_{\tau r}^2$  for  $z_{\Delta}^+$  between  $\ell_T u_{\tau r} / \nu_r$  and  $\delta'_r u_{\tau r} / \nu_r$ , then the last term in (A9) vanishes. This only happens at matched  $Re_{\tau}$  as well. So the sources of error are from the normalised  $-dP/dx$  and from the  $-\overline{u'w'}$  term. And if we assume that the friction Reynolds numbers are matched between the riblet and smooth wall, such that  $\delta'_r u_{\tau r} / \nu_r = \delta_s u_{\tau s} / \nu_s$ , then  $\epsilon_{\Delta}^+ = 0$ . Therefore, from (A9), we have  $\Delta U^+ = -(U_{R0} / u_{\tau r} - U_{SC} / u_{\tau s})$ , where the roughness function is irrespective of  $z_{\Delta}^+$ . For  $U_{R0} / u_{\tau r}$ , evaluating the mean velocity at the crest may not be accurate because the effect due to the texture (inhomogeneity) is still present at the crest. Figure 20 illustrates the method used to determine  $U_{R0} / u_{\tau r}$ .

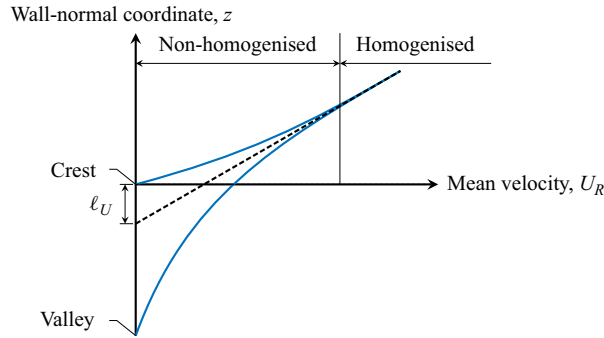


Figure 20. The mean velocity profiles above the riblet crest and the valley are homogenised (collapse) above the riblet crest. We measure  $\ell_U$  as the distance relative to the crest of the origin of the linearly extrapolated homogenised mean velocity (depicted as the dashed line) with a gradient measured locally at  $zu_{\tau r}/\nu_r \approx 1$ .

Here, the homogenised mean flow perceives a virtual origin at  $\ell_U u_{\tau r}/\nu_r$  below the crest when linearly extrapolated to  $U_R = 0$  with a gradient measured locally at  $zu_{\tau r}/\nu_r \approx 1$ . For small, smooth-wall-like riblets, the viscous-scaled gradient is close to 1, and thereby,  $U_{R0}/u_{\tau r} \approx \ell_U u_{\tau r}/\nu_r$ . For  $U_{SC}/u_{\tau r}$ , we assume from (A8) that  $\ell_T u_{\tau r}/\nu_r$  is small such that the second and third term can be neglected (i.e. unity gradient), such that  $U_{SC}/u_{\tau s} = \ell_T u_{\tau r}/\nu_r$ . Hence, we have

$$\Delta U^+ = - \left( \frac{\ell_U u_{\tau r}}{\nu_r} - \frac{\ell_T u_{\tau r}}{\nu_r} \right). \tag{A10}$$

Equation (A10) is an idealistic equation assuming collapsed Reynolds stress and friction Reynolds number. However, this condition is not true from the DNS because the channel height is measured from the riblet mean height, and not the turbulence origin. Based on the simulations performed as per figure 19, the friction Reynolds number is not matched,  $\delta_s u_{\tau s}/\nu_s \neq \delta_r' u_{\tau r}/\nu_r$  so the error  $\epsilon_{\Delta}^+$  in (A9) remains. Another error arises from the inequality of Reynolds stresses  $-\overline{u'w'_S}/u_{\tau s}^2 \neq -\overline{u'w'_R}/u_{\tau r}^2$ , typically for larger  $\ell_g u_{\tau r}/\nu_r$  riblets. And finally, a statistical error,  $\pm \zeta$  (2.2) due to the minimal channel exist in (A7a,b), prior to the subtraction in (A9). The error,  $\pm \zeta$  can be minimised by increasing the sampling time. By removing the error due to unmatched  $Re_{\tau}$ , we can recover the actual  $\Delta U^+$ , plus minor errors due to the aforementioned sources.

## Appendix B. Calibration of model parameters

### B.1. Domain height

We demonstrate that the predictions of the viscous vortex model ( $\ell_{T,VV}^+$ ) remain nearly constant when a domain height in the range of  $10 \leq H^+ \leq 15$  is selected. Table 3 summarises the corresponding  $\ell_{T,VV}^+$  values based on prescribed parameters ( $B/A$  and  $\Phi$ ) extracted from the DNSs of smooth walls at various heights ranging from  $10 \leq z^+ \leq 15$ . Here, we observe that  $\ell_{T,VV}^+$  varies by approximately 3% among the prescribed domain heights, indicating that any of these parameters would be suitable. For our analysis, we select the parameters corresponding to  $z^+ = 12$ , with the respective  $\ell_{T,VV}^+$  (and  $\Delta U_{VV}^+$ ) reported in figures 16–18. Furthermore, the modelled  $\ell_{T,VV}^+$  values closely align with  $\ell_T^+$  values from DNSs. The riblets listed in table 3 are matched with the optimal riblet cases





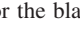

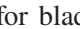

$z^+$	$B/A$	$\Phi$	$\ell_{T,VV}^+$	
				
10	1.70	$0.35\pi$	0.88213	1.46590
11	1.50	$0.33\pi$	0.88956	1.47656
12	1.40	$0.31\pi$	0.89928	1.49131
13	1.30	$0.29\pi$	0.90435	1.49855
14	1.25	$0.26\pi$	0.90979	1.50669
15	1.20	$0.24\pi$	0.91120	1.50818

Table 3. Summary of the viscous vortex model turbulence origin predictions  $\ell_{T,VV}^+$ , calculated using various domain heights  $z^+$ , alongside the corresponding prescribed parameters  $B/A$  and  $\Phi$  extracted from DNS. Riblet size is  $\ell_g^+ \approx 10$ :  $s^+ = 15.6$  for blade riblets () and  $s^+ = 14.7$  for trapezoidal riblets (). The calculated  $\ell_{T,VV}^+$  are virtually insensitive to the domain height (varying by less than 3% for  $10 \leq z^+ \leq 15$ ), and are close to that from the DNS:  $\ell_T^+ \approx 0.95$  for the blade riblet () and  $\ell_T^+ \approx 1.49$  for the trapezoidal riblet ()

at  $\ell_g^+ \approx 10$ , where the DNS results for blade riblets () yield  $\ell_T^+ \approx 0.95$  and the trapezoidal riblets () yield  $\ell_T^+ \approx 1.49$ , resulting in a difference of 1%–8%.

### B.2. Wavelength and amplitude

We also demonstrate that, by setting  $\lambda_y^+ = 50$  (along with the corresponding  $A$ ,  $B$  and  $\Phi$  at  $z^+ = 12$ ), the viscous vortex model provides the most accurate prediction of  $\ell_T^+$ , compared with the (sub)harmonics,  $\lambda_y^+ = 25$  and  $100$ . Comparisons with the measured virtual origins from DNSs of both trapezoidal riblets and slip/transpiration surfaces (Ibrahim *et al.* 2021; Habibi Khorasani *et al.* 2022) allow us to calibrate the model with diverse wall conditions and with a larger  $\ell_T^+$  range of  $0.5 \lesssim \ell_T^+ \lesssim 5$ . The spanwise slip and transpiration lengths ( $\ell_y^+$ ,  $\ell_z^+$ ) are applied through the same Robin boundary condition as the DNSs of Ibrahim *et al.* (2021),  $v|_{z=0} = \ell_y \partial v / \partial z|_{z=0}$  and  $w|_{z=0} = \ell_z \partial w / \partial z|_{z=0}$ . From the DNSs conducted by Habibi Khorasani *et al.* (2022), the wall-normal velocity at  $z = 0$  is  $w|_{z=0} = -m_x \partial u / \partial x|_{z=0} - m_y \partial v / \partial y|_{z=0}$ , where  $m_x$  and  $m_y$  are the prescribed constants. When  $m_x = m_y$ , this condition is equivalent to Ibrahim *et al.* (2021), leading to  $\ell_z = m_x = m_y$  by continuity. Figure 21 compares the values of  $\ell_{T,VV}^+$  obtained from the viscous vortex model (using the parameters corresponding to the respective  $\lambda_y^+$ ) with the turbulence virtual origins  $\ell_T^+$  measured from the DNSs. The slip/transpiration DNS cases correspond to the regime where  $\ell_v^+ \approx \ell_w^+$ , ensuring that the DNS  $\omega_x^+$  matches well with the smooth-wall data from at least the local minimum (i.e. at  $z^+ \approx 5$ ) and above, as observed by Gómez-de-Segura & García-Mayoral (2020). This allows for direct comparison with viscous vortex predictions. The results for  $\lambda_y^+ = 50$ , as shown in figure 21(b), demonstrate that the viscous vortex model provides a more accurate prediction of  $\ell_T^+$  compared with  $\lambda_y^+ = 25$  or  $100$ .

The amplitude ratio of the boundary condition  $B/A = 1.4$  is obtained by averaging the segmented Fourier signals (see § 4.2). Note that the model turbulence offset  $\ell_{T,VV}^+$  is invariant of the magnitudes of  $A$  and  $B$ , as long as their ratio  $B/A$  remains the same, due to the linearity of the Stokes equations. When we compute  $A$  and  $B$  by averaging the

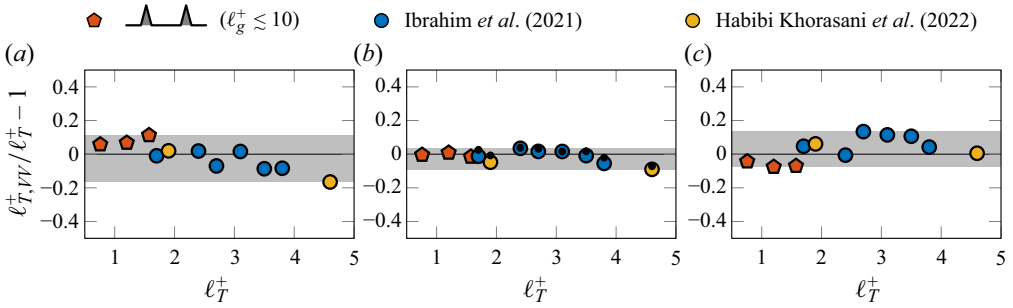


Figure 21. Comparison of the DNS turbulence virtual origins  $l_T^+$  of trapezoidal riblets ( $\blacktriangle$ ) and slip surfaces of Ibrahim *et al.* (2021) and Habibi Khorasani *et al.* (2022) with the results obtained from the viscous vortex model, denoted as  $l_{T,VV}^+$ . The parameters used in the model are extracted from the smooth-wall DNSs at a height of  $z^+ \approx 12$  and wavelengths of (a)  $\lambda_y^+ = 25$  using  $B/A = 0.86$  and  $\Phi = 0.24\pi$ , (b)  $\lambda_y^+ = 50$  using  $B/A = 1.4$  and  $\Phi = 0.31\pi$  and (c)  $\lambda_y^+ = 100$  using  $B/A = 2.5$  and  $\Phi = 0.34\pi$ . Black markers ( $\bullet$ ) in (b) show model prediction using  $B/A = 1.1$ .

wider, non-segmented Fourier signals instead, we obtain a slightly smaller  $B/A \approx 1.1$  but the same  $\Phi \approx 0.31\pi$ .

We can use the viscous vortex model to check the consistency between these two DNS-obtained  $B/A$ . In terms of the prediction of  $l_T^+$ , the ratio  $B/A = 1.1$  (with the same  $\lambda_y^+ = 50$ ,  $z^+ = 12$  and  $\Phi = 0.31\pi$ ) results in insignificant changes to  $l_{T,VV}^+$  ( $\bullet$ , figure 21). However, in terms of the model r.m.s. vorticity profile, we observe a local minimum at  $z_{\omega_x,min}^+ \approx 4.9$  when  $B/A = 1.4$  and  $z_{\omega_x,min}^+ \approx 5.5$  when  $B/A = 1.1$ . The local minimum of the DNS r.m.s. vorticity profile is at  $z_{\omega_x,min}^+ \approx 5$  (e.g. Kim *et al.* 1987), highlighting the advantage of segmenting the signals when obtaining  $B/A$ .

### Appendix C. Analytical viscous vortex solutions at various spanwise shifts of the wall using Floquet–Bloch decomposition

In the viscous vortex model, we account for the spanwise shifts ( $\Delta$ ) of the vortex above riblet walls based on the unpinned character of quasi-streamwise vortices (see figure 11). This step requires multiple solutions between  $0 \leq \Delta < s$ , which may be time consuming depending on the interval sizes of  $\Delta$ . Following from the Floquet–Bloch decomposition, we can instead analytically find the solution field for any  $\Delta$  from two linearly independent solutions

$$\begin{aligned} \{v_\theta, w_\theta, \omega_{x,\theta}\}(\theta, \eta, z) &= C(\theta) \left\{ v_{\tilde{\theta}}, w_{\tilde{\theta}}, \omega_{x,\tilde{\theta}} \right\}(\tilde{\theta} = 0, \eta, z) \\ &+ D(\theta) \left\{ v_{\tilde{\theta}}, w_{\tilde{\theta}}, \omega_{x,\tilde{\theta}} \right\}(\tilde{\theta} = \theta_0, \eta, z), \end{aligned} \quad (C1)$$

where  $\theta = 2\pi\Delta/\lambda_y$  is a variable associated with the desired solution and  $\tilde{\theta}$  is a chosen constant associated with the independent solutions. For the first independent solution, we choose  $\tilde{\theta} = 0$ , whilst for the second independent solution, we choose  $\tilde{\theta} = \theta_0 = (2\pi/\lambda_y)(s/2)$  (half-riblet spacing). We find  $C$  and  $D$  by substituting the left-hand side of (C1) with the boundary velocity at the top (see figure 11) to find

$$C = \cos \theta - \frac{\sin \theta}{\tan \theta_0} \quad D = \frac{\sin \theta}{\sin \theta_0}, \quad (C2a,b)$$



where  $\theta_0 \neq n\pi$  for any integer  $n$  to avoid a zero division. To ensure that the second solution is independent, we choose the aforementioned  $\theta_0 = (2\pi/\lambda_y)(s/2)$ , i.e. shift of half a riblet period. Because  $\theta_0 \neq n\pi$ , our choice of  $\theta_0 = (2\pi/\lambda_y)(s/2)$  gives  $\lambda_y \neq s/n$ , which means  $\lambda_y > s$ . Since we use  $\lambda_y^+ = 50$  for the viscous vortex model, the spacings for small riblets ( $\ell_g^+ \lesssim 10.7$ ) are all smaller than  $\lambda_y^+$  ( $s^+ < 20$ , see table 2) and hence, our choice of  $\theta_0 = (2\pi/\lambda_y)(s/2)$  will work for all small riblets. Using (C1) and (C2a,b), we can analytically compute the solution for any  $\Delta$ . The uniform average can then be computed using (4.8) by substituting  $\eta$  with  $y$ , i.e. changing the reference frame from the riblets ( $\eta$ ) to the top velocity boundary condition ( $y$ ).

#### REFERENCES

- BANNIER, A., GARNIER, E. & SAGAUT, P. 2015 Riblet flow model based on an extended FIK identity. *Flow Turbul. Combust.* **95**, 351–376.
- BECHERT, D.W., BRUSE, M. & HAGE, W. 2000 Experiments with three-dimensional riblets as an idealized model of shark skin. *Exp. Fluids* **28**, 403–412.
- BECHERT, D.W., BRUSE, M., HAGE, W., VAN DER HOEVEN, J.G.T. & HOPPE, G. 1997 Experiments on drag-reducing surfaces and their optimization with an adjustable geometry. *J. Fluid Mech.* **338**, 59–87.
- BENDER, C.M. & ORSZAG, S.A. 1978 *Advanced Mathematical Methods for Scientists and Engineers*. McGraw-Hill.
- BOTTARO, A. 2019 Flow over natural or engineered surfaces: an adjoint homogenization perspective. *J. Fluid Mech.* **877**, P1.
- BUSHNELL, D.M. 2003 Aircraft drag reduction—a review. *Proc. Inst. Mech. Engrs* **217**, 1–18.
- CHAPMAN, D. & KUHN, G. 1986 The limiting behaviour of turbulence near a wall. *J. Fluid Mech.* **170**, 265–292.
- CHAVARIN, A & LUHAR, M. 2020 Resolvent analysis for turbulent channel flow with riblets. *AIAA J.* **58**, 589–599.
- CHOI, H., MOIN, P. & KIM, J. 1993 Direct numerical simulation of turbulent flow over riblets. *J. Fluid Mech.* **255**, 503–539.
- CHOI, K.S. 1989 Near-wall structure of a turbulent boundary layer with riblets. *J. Fluid Mech.* **208**, 417–458.
- CHOI, K.S. 2013 Smart flow control with riblets. *Adv. Mater. Res.* **745**, 27–40.
- CHUNG, D., CHAN, L., MACDONALD, M., HUTCHINS, N. & OOI, A. 2015 A fast direct numerical simulation method for characterising hydraulic roughness. *J. Fluid Mech.* **773**, 418–431.
- CIPELLI, S. 2023 Efficient direct numerical simulations of straight and sinusoidal riblets in turbulent channel flows. Master's thesis, Politecnico di Milano.
- COLES, D.E. 1978 A model for flow in the viscous sublayer. In *Workshop on Coherent Structures of Turbulent Boundary Layers, AFOSR/Lehigh University, Bethlehem, PA* (ed. C.R. Smith & D.E. Abbott), pp. 462–475.
- VON DEYN, L.H., GATTI, D. & FROHNAPFEL, B. 2022 From drag-reducing riblets to drag-increasing ridges. *J. Fluid Mech.* **951**, A16.
- EL-SAMNI, O.A., CHUN, H.H. & YOON, H.S. 2007 Drag reduction of turbulent flow over thin rectangular riblets. *Intl J. Engng Sci.* **45**, 436–454.
- ENDRIKAT, S., MODESTI, D., GARCÍA-MAYORAL, R., HUTCHINS, N. & CHUNG, D. 2021a Influence of riblet shapes on the occurrence of Kelvin–Helmholtz rollers. *J. Fluid Mech.* **913**, A37.
- ENDRIKAT, S., MODESTI, D., MACDONALD, M., GARCÍA-MAYORAL, R., HUTCHINS, N. & CHUNG, D. 2021b Direct numerical simulations of turbulent flow over various riblet shapes in minimal-span channels. *Flow Turbul. Combust.* **107**, 1–29.
- ENDRIKAT, S., NEWTON, R., MODESTI, D., GARCÍA-MAYORAL, R., HUTCHINS, N. & CHUNG, D. 2022 Reorganisation of turbulence by large and spanwise-varying riblets. *J. Fluid Mech.* **952**, A27.
- FAIRHALL, C.T., ABDERRAHAMAN-ELENA, N. & GARCÍA-MAYORAL, R. 2019 The effect of slip and surface texture on turbulence over superhydrophobic surfaces. *J. Fluid Mech.* **861**, 88–118.
- FLORES, O. & JIMÉNEZ, J. 2010 Hierarchy of minimal flow units in the logarithmic layer. *Phys. Fluids* **22**, 071704.
- GARCÍA-MAYORAL, R., GÓMEZ-DE-SEGURA, G. & FAIRHALL, C.T. 2019 The control of near-wall turbulence through surface texturing. *Fluid Dyn. Res.* **51**, 011410.
- GARCÍA-MAYORAL, R. & JIMÉNEZ, J. 2011a Drag reduction by riblets. *Phil. Trans. R. Soc. Lond. A* **369**, 1412–1427.

- GARCÍA-MAYORAL, R. & JIMÉNEZ, J. 2011*b* Hydrodynamic stability and breakdown of the viscous regime over riblets. *J. Fluid Mech.* **678**, 317–347.
- GARCÍA-MAYORAL, R. & JIMÉNEZ, J. 2012 Scaling of turbulent structures in riblet channels up to  $Re_\tau \approx 550$ . *Phys. Fluids* **24**, 105101.
- GARRATT, J.R. 1990 The internal boundary layer – a review. *Boundary-Layer Meteorol.* **50**, 171–203.
- GOLDSTEIN, D.B., HANDLER, R. & SIROVICH, L. 1995 Direct numerical simulation of turbulent flow over a modelled riblet covered surface. *J. Fluid Mech.* **302**, 333–376.
- GOLDSTEIN, D.B. & TUAN, T.-C. 1998 Secondary flow induced by riblets. *J. Fluid Mech.* **363**, 115–151.
- GÓMEZ-DE-SEGURA, G., FAIRHALL, C.T., MACDONALD, M., CHUNG, D. & GARCIA-MAYORAL, R. 2018*a* Manipulation of near-wall turbulence by surface slip and permeability. *J. Phys.: Conf. Ser.* **1001**, 012011.
- GÓMEZ-DE-SEGURA, G. & GARCÍA-MAYORAL, R. 2020 Imposing virtual origins on the velocity components in direct numerical simulations. *Intl J. Heat Fluid Flow* **86**, 108675.
- GÓMEZ-DE-SEGURA, G., SHARMA, A. & GARCÍA-MAYORAL, R. 2018*b* Virtual origins in turbulent flows over complex surfaces. In *Centre for Turbulence Research Proceedings of the Summer Program 2018* (ed. P. Moin & J. Urzay), pp. 277–286. Stanford University.
- GRÜNEBERGER, R. & HAGE, W. 2011 Drag characteristics of longitudinal and transverse riblets at low dimensionless spacings. *Exp. Fluids* **50**, 363–373.
- HABIBI KHORASANI, S.M., LĀCIS, U., PASCHE, S., ROSTI, M.E. & BAGHERI, S. 2022 Near-wall turbulence alteration with the transpiration-resistance model. *J. Fluid Mech.* **942**, A45.
- HAM, F., MATTSSON, K. & IACCARINO, G. 2006 Accurate and stable finite volume operators for unstructured flow solvers. In *Center for Turbulence Research, Stanford University/NASA AMES, Annual Research Briefs* (ed. P. Moin & N.N. Mansour), pp. 243–261. Stanford University.
- HAM, F., MATTSSON, K., IACCARINO, G. & MOIN, P. 2007 Towards time-stable and accurate LES on unstructured grids. In *Complex Effects in Large Eddy Simulations* (ed. S.C. Kassinis, C.A. Langer, G. Iaccarino & P. Moin), pp. 235–249. Springer.
- IBRAHIM, J., GÓMEZ-DE-SEGURA, G., CHUNG, D. & GARCÍA-MAYORAL, R. 2021 The smooth-wall-like behaviour of turbulence over drag-altering surfaces: a unifying virtual-origin framework. *J. Fluid Mech.* **915**, A56.
- JEONG, J., HUSSAIN, F., SCHOPPA, W. & KIM, J. 1997 Coherent structures near the wall in a turbulent channel flow. *J. Fluid Mech.* **332**, 185–214.
- JIMÉNEZ, J. 1994 On the structure and control of near wall turbulence. *Phys. Fluids* **6**, 944–953.
- JIMÉNEZ, J. 2018 Coherent structures in wall-bounded turbulence. *J. Fluid Mech.* **842**, P1.
- JIMÉNEZ, J., DEL ÁLAMO, J.C. & FLORES, O. 2004 The large-scale dynamics of near-wall turbulence. *J. Fluid Mech.* **505**, 179–199.
- JIMÉNEZ, J. & MOIN, P. 1991 The minimal flow unit in near-wall turbulence. *J. Fluid Mech.* **225**, 213–240.
- KIM, J., MOIN, P. & MOSER, R. 1987 Turbulence statistics in fully developed channel flow at low Reynolds number. *J. Fluid Mech.* **177**, 133–166.
- KLINE, S., REYNOLDS, W., SCHRAUB, F. & RUNSTADLER, P. 1967 The structure of turbulent boundary layers. *J. Fluid Mech.* **30**, 741–773.
- LAUGA, E. & STONE, H.A. 2003 Effective slip in pressure-driven Stokes flow. *J. Fluid Mech.* **489**, 55–77.
- LEE, S.-J. & LEE, S.-H. 2001 Flow field analysis of a turbulent boundary layer over a riblet surface. *Exp. Fluids* **30**, 153–166.
- LI, M., DE SILVA, C.M., ROUHI, A., BAIDYA, R., CHUNG, D., MARUSIC, I. & HUTCHINS, N. 2019 Recovery of wall-shear stress to equilibrium flow conditions after a rough-to-smooth step change in turbulent boundary layers. *J. Fluid Mech.* **872**, 472–491.
- LI, W. & LIU, H. 2019 Two-point statistics of coherent structures in turbulent flow over riblet-mounted surfaces. *Acta Mechanica Sin.* **35**, 457–471.
- LOZANO-DURÁN, A. & JIMÉNEZ, J. 2014 Effect of the computational domain on direct simulations of turbulent channels up to  $Re_\tau = 4200$ . *Phys. Fluids* **26**, 011702.
- LUCHINI, P. 1996 Reducing the turbulent skin friction. In *Computational Methods in Applied Sciences '96* (ed. J.A. Désidéri *et al.*), pp. 466–470.
- LUCHINI, P., MANZO, F. & POZZI, A. 1991 Resistance of a grooved surface to parallel flow and cross-flow. *J. Fluid Mech.* **228**, 87–109.
- LUNDGREN, T.S. 1982 Strained spiral vortex model for turbulent fine structure. *Phys. Fluids* **25**, 2193–2203.
- MACDONALD, M., CHUNG, D., HUTCHINS, N., CHAN, L., OOI, A. & GARCÍA-MAYORAL, R. 2017 The minimal-span channel for rough-wall turbulent flows. *J. Fluid Mech.* **816**, 5–42.
- MALATHI, A.S., NARDINI, M., VAID, A., VADLAMANI, N.R. & SANDBERG, R.D. 2022 On the efficacy of riblets toward drag reduction of transitional and turbulent boundary layers. *AIAA Paper 2022-0472*.

*A viscous vortex model for riblet drag reduction predictions*

- MINNICK, B. 2022 A restricted nonlinear approach to momentum and scalar mixing in wall-turbulence. PhD thesis, Johns Hopkins University.
- MODESTI, D., ENDRIKAT, S., HUTCHINS, N. & CHUNG, D. 2021 Dispersive stresses in turbulent flow over riblets. *J. Fluid Mech.* **917**, A55.
- POLLARD, A., SAVILL, A.M., TULLIS, S. & WANG, X. 1994 Simulating turbulent flow over thin element and flat valley V-shaped riblets. *AIAA J.* **34**, 2261–2268.
- PULLIN, D.I. & SAFFMAN, P.G. 1993 On the Lundgren–Townsend model of turbulent fine scales. *Phys. Fluids* **5**, 126–145.
- RAN, W., ZARE, A. & JOVANOVIĆ, M. 2021 Model-based design of riblets for turbulent drag reduction. *J. Fluid Mech.* **906**, A7.
- ROBINSON, S.K. 1991 The kinematics of turbulent boundary layer structure. PhD thesis, NASA, TR TM-103859.
- SCHLATTER, P., LI, Q., ÖRLÜ, R., HUSSAIN, F. & HENNINGSON, D.S. 2014 On the near-wall vortical structures at moderate Reynolds numbers. *Eur. J. Mech. (B/Fluids)* **48**, 75–93.
- SCHULTZ, M.P., BENDICK, J.A., HOLM, E.R. & HERTEL, W.M. 2011 Economic impact of biofouling on a naval surface ship. *Biofouling* **27**, 87–98.
- SMITH, B.R., YAGLE, P. & MCCLURE, P.D. 2023 Computational simulation of staggered 3-D riblets for skin friction drag reduction. *AIAA Paper* 2023-1763.
- SMITH, C.R. & METZLER, S.P. 1983 The characteristics of low-speed streaks in the near-wall region of a turbulent boundary layer. *J. Fluid Mech.* **129**, 27–54.
- SPALART, P.R. & MCLEAN, J.D. 2011 Drag reduction: enticing turbulence, and then an industry. *Phil. Trans. R. Soc. Lond. A* **369**, 1556–1569.
- SPALDING, D.B. 1961 A single formula for the ‘law of the wall’. *Trans. ASME J. Appl. Mech.* **28**, 455–457.
- VINUESA, R., PRUS, C., SCHLATTER, P. & NAGIB, H.M. 2016 Convergence of numerical simulations of turbulent wall-bounded flows and mean cross-flow structure of rectangular ducts. *Meccanica* **51**, 3025–3042.
- VISWANATH, P.R. 2002 Aircraft viscous drag reduction using riblets. *Prog. Aerosp. Sci.* **38**, 571–600.
- WALSH, M.J. 1982 Turbulent boundary layer drag reduction using riblets. *AIAA Paper* 1982-0169.
- WALSH, M.J. 1990 Effect of detailed surface geometry on riblet drag reduction performance. *J. Aircraft* **27**, 572–573.